Lithological control on the post-orogenic topography and erosion history of the Pyrenees

Lithological control on the post-orogenic topography and erosion history of the Pyrenees.

Thomas Bernard[1]*, Hugh D. Sinclair[1], Boris Gailleton[1], Simon M. Mudd[1], Mary Ford[2]

(1) School of GeoSciences, The University of Edinburgh, Drummond Street, Edinburgh, EH8 9XP, UK
(2) Centre de Recherches Pétrographiques et Géochimiques (CRPG), Université de Lorraine, Nancy, France

*Corresponding author: thomas.bernard@ed.ac.uk

ABSTRACT:

Numerous studies on active mountain ranges have demonstrated the interaction between tectonics and climate in shaping topography. Here we explore how variations in rock types have affected the topographic development of the Pyrenees since cessation of orogenesis ca. 20 Ma. Our study is based on a multidisciplinary approach and integrates topographic analyses, rock strength measurements and thermal modelling of low-temperature thermochronological data published across the Central Pyrenees. Results indicate a strong influence of rock strength in determining the post-orogenic morphology of the Pyrenees. We observe a correlation between rock strength and the normalized channel steepness index (k_{sn}) of the different lithologies. Moreover, the highest topography is dominated by the Variscan plutonic massifs which have highest rock strength. Consequently, the drainage divide appears to track the position of these massifs. Abrupt deceleration of exhumation recorded in inverse modelling of low-temperature thermochronologic data suggests that the exhumation of the Variscan massifs also played role in lowering in erosion rates over the massifs during orogenesis.

KEYWORDS:

Pyrenees, channel steepness, rock strength, thermal histories, landscape evolution, exhumation.

1. Introduction

The topographic elevation and relief of active mountain ranges have long been recognised to reflect the long-term competition between tectonic and surface process linked to climate (Beaumont et al., 2001). The macro-geomorphic form of many active mountain chains such as the Southern Alps of

New Zealand, the Andes and Taiwan have been reproduced through numerical modelling of tectonically forced rock trajectories countered by erosion (e.g. Koons, 1990). However, most of the mountain ranges in the world seem to be in various stages of post-orogenic decay such as the European Alps, Urals, Caledonides, Appalachians or Pyrenees (Baldwin et al., 2003; Tucker and Van der Beek, 2013). Underpinning the transition to a post-orogenic state is the competition between erosion and crustal thickening. We consider post-orogenesis as the time at which erosion is dominant over crustal thickening and hence is characterised by regional isostatic rebound, and so during the early stages of post-orogenesis, structural deformation may continue. This definition avoids debate over the timing of cessation of fault movement in the range which may continue after net shortening has stopped. These processes do not include epeirogenic vertical motions forced by mantle flow (e.g. dynamic topography) although it is recognized that slab detachment and mantle processes can impact late stage orogenesis as interpreted in the south-eastern Carpathian (Matenco, 2017). The landscape evolution of these decaying mountains, where the switch from localised fault-controlled rock uplift to more regional isostatic controls, should be relatively simple with progressive and relatively uniform erosion resulting in a general lowering of both elevation and topographic relief (Baldwin et al., 2003; Tucker and Van der Beek, 2013). In the absence of fault activity, this evolution may be perturbed by external erosional drivers or intrinsic characteristics such as base-level variations, drainage capture, dynamic topography, climate change or lithological variations (Valla et al., 2012; Flowers and Ehlers, 2018). The role of rock strength in moderating stress fields and erosion rates in active mountain ranges has been difficult to characterise (Koons et al., 2012). In contrast, in post-orogenic settings, the influence of rock strength can be more clearly isolated as proposed from the Cape Mountains of South Africa (Scharf et al., 2013) where low denudation rates and the maintenance of topography is primarily attributed to the presence of robust quartzites that constitute the backbone of the range.

Long-term erosion rates in active or inactive mountain ranges are largely limited by the ability of rivers to erode into bedrock, which is governed by the processes of plucking and abrasion of the river bed (Whipple et al., 2000). The former is largely a function of fracture density, and the latter of tensile strength. Experimental studies demonstrate that lithologies with contrasting tensile strength influence the erosion rate along fluvial channels (Sklar and Dietrich, 2001). Several studies have used the stream

power model to demonstrate that rock strength could cause variations in erosion rates by a factor of 3 to 5 depending on the range of lithologies (Sklar and Dietrich, 2001). Plucking is influenced by the presence and orientation of joints, beddings, faults, or foliation impacting the erodibility of rock (Whipple et al., 2000). Flowers and Ehlers (2018) show that thermochronological data and associated thermal histories can be strongly affected by changes of erosion rates caused by variations in the erodibility of rock, typically after removal of sedimentary cover and exposure of underlying crystalline basement. Glotzbach et al. (2011) show, for example, that decreases in exhumation rates at 6 ± 2 Ma in the Western Alps can be associated to a general decrease in convergence rates and/or extensive exposure of less erodible rock types.

Here, we explore the influence of rock strength on the modern topography of the Pyrenees at the border between France and Spain (Fig. 1). The Pyrenees have been dominated by post-orogenic decay for the last ca. 20 Myr (Meigs et al., 1996; Sinclair et al., 2005). In this study we measure the tensile strength of the main lithologies across the range, and compare this to the normalised channel steepness (e.g., Wobus et al., 2006) derived from measurement of the χ parameter (Perron and Royden, 2013). We compare the rock strength to channel steepness, and determine the role of lithology in defining the modern drainage divide across the range. Finally, we explore the potential effect of unroofing lithologies with varying rock strengths on the evolution of the cooling/exhumation history during growth of the range. Our results demonstrate that lithology is a fundamental control on the topographic form and elevation of the modern Pyrenees, and that it may have played a key control on the history and distribution of erosion during orogenesis.

2. Geologic background

2.1. Geology

The Pyrenees form a 450 km topographic long barrier that runs from the Mediterranean Sea (Cap de Creus) to the Bay of Biscay (Cap Higher) with a 150 km-wide central region that separates the Iberian Peninsula from the European continent (Fig. 1). The Pyrenees extend as a generally linear east-

west orographic barrier with a climatic asymmetry across the range. The Northern Pyrenees are characterised by a relatively steep, wet flank compared to the broader semi-arid southern flank. This morphology has been inherited from the distinct growth of the southern side as an accretionary pro-wedge and the north as a retro-wedge (Beaumont et al., 2000; Sinclair et al., 2005). The formation of the Pyrenees resulted from the convergence and collision of the Iberian and European plates from late Cretaceous to early Miocene time (Roest and Srivastava, 1991). The geodynamical expression of this convergence is the formation of a doubly-vergent collisional orogen, which accommodates up to 165 km of shortening reflected in upper crustal thickening (Munoz, 1992; Beaumont et al., 2000).

The Pyrenees can be divided into a series of five main tectonic units (Fig. 1), which, from south to north, are: the Ebro pro-foreland basin, the South Pyrenean Thrust Belt, the Axial Zone, the North Pyrenean Thrust Belt and the Aquitaine retro-foreland basin (Munoz, 1992; Vergés et al., 1995).

The Ebro foreland basin was initiated in Paleocene times and consists of marine successions of Paleocene to early Priabonian age, and continental successions of early Priabonian to mid- Oligocene age. The South Pyrenean Thrust Belt is made up mainly by a Mesozoic platform series and Palaeogene rocks (Munoz, 1992) and in the Central Pyrenees consist of three main thrust sheets, named from south to north: Sierra Marginales, Montsec and Boixols.

The Axial zone is separated from the North Pyrenean Thrust Belt by the North Pyrenean fault zone, which corresponds to the present boundary between the Iberian and European continent (Verges and Munoz, 1990). The Axial zone is composed of three Variscan basement thrust sheets named from north to south, the Rialp, Orri and Nogueres thrust sheets (Munoz, 1992). These units comprise thick Precambrian and Paleozoic metamorphosed sedimentary successions intruded by Variscan granitoid massifs.

The North Pyrenean Thrust Belt and Aquitaine Basin constitute the retro-wedge and retro-foreland basin of the Pyrenees respectively. The North Pyrenean Thrust System involves Variscan basement massifs (called the North Pyrenean Massifs such as the Trois-Seigneurs and Ariège massifs) and Mesozoic to lower Eocene sedimentary cover rock. The Aquitaine basin formed from Late Cretaceous to Miocene by flexure of the upper plate in response to the load the North Pyrenean Thrust Belt (Brunet, 1986).

90

91 *2.2. Exhumation history*

92 The transition from syn-orogenic shortening to post-orogenic quiescence in the Pyrenees is
93 associated with the last evidence of differential exhumation across thrust faults in the Axial Zone
94 revealed by low temperature thermochronology at around 20 Ma (Gibson et al; 2007; Jolivet et al.
95 2007). Post-orogenic exhumation of the South Pyrenean Thrust Belt is recorded by apatite (U+Th)/He
96 thermochronology (AHe) analysis at ca. 20 Ma to present time (Fillon et al., 2013). A late stage
97 acceleration in exhumation around 9 Ma has been linked to the reconnection of the Ebro Basin to the
98 Mediterranean Sea causing evacuation of a thick sedimentary succession that draped the South
99 Pyrenean Thrust Belt (Coney et al., 1996; Fillon et al., 2013).

100 Initial analyses of low-temperature thermochronology in the Pyrenees used single-elevation
101 samples on basement and granitic massifs. Yelland et al., (1990) highlight a contrast in the apatite
102 fission track ages (AFTA) and mean track length (MTL) between the south and north and interpret it as
103 recording an initial period of rapid Palaeocene-Eocene exhumation in the northern Pyrenees followed
104 by a protracted period of less rapid exhumation in the southern Pyrenees. Morris et al. (1998) performed
105 subsequent modelling of the data from Yelland et al. (1990) to demonstrate a syn-orogenic sediment
106 discharge that was 1.5 to 2.8 times greater to the south than to the north. By using multiple vertical
107 profiles from granitic massifs in the Pyrenees (Maladeta, Riberot and Lacourt), Fitzgerald et al. (1999)
108 showed an asymmetric exhumation with AFT ages younging from north to south across the Pyrenees.
109 Sinclair et al. (2005) demonstrated that the core of the Axial Zone records the greatest depth of
110 exhumation and that there was a progressive southward shift with highest exhumation rates associated
111 to the growth of the antiformal stack from 36 to 20 Ma. Gibson et al., (2008) show the youngest evidence
112 for accelerated differential exhumation at ~20 Ma on the southern Axial Zone. Finally, exhumation of
113 the northern central Pyrenees has also been recorded by Vacherat et al. (2016) showing that the Trois-
114 Seigneurs, Lacourt and Foix massifs record monotonic cooling starting at ~50 Ma and lasting until ~35
115 Ma.

116

117 **3. Methodology**

3.1. Topographic analysis

Incision of river channels underpins the topographic evolution of landscapes. Moreover, river morphologies record information about external controlling factors such as vertical displacements of rock, climate and intrinsic characteristics such as lithology. The seminal work of Gilbert (1877), suggested that erosion rates in bedrock rivers are proportional to a combination of channel gradient and water discharge. Gilbert (1877) recognised that changing discharge will affect channel steepness, noting that if all else is equal, channels with more water will have gentler gradients. Authors began quantifying the relationship between channel gradients and drainage area (a proxy for discharge) in the middle of the 20th century and Morisawa (1962) recognised that this relationship could be described by a power law. We can state this power law as:

$$S = k_s A^{-\theta}, \quad (1)$$

where S is the topographic slope (dimensionless), k_s is a steepness index ($m^{2\theta}$), A is the drainage area (m^2) and θ is called the "concavity index" (dimensionless). Numerous authors have found that the steepness index scales with erosion rate in rivers underlain by a homogenous lithology (see compilations in Kirby and Whipple, 2012 and Harel et al., 2016). Extraction of the steepness index from topographic data typically involves selecting a fixed value for the concavity index, called the reference concavity, and then extracting the "normalized" steepness index (k_{sn}) from slope-area data (e.g., Wobus et al., 2006; Kirby and Whipple, 2012). A drawback of this approach is that channel gradient data can be noisy and drainage areas tend to be discontinuous due to channel junctions, and so extraction of k_{sn} from slope-area data requires a number of data smoothing techniques (e.g., Wobus et al., 2006).

An alternative approach, is to integrate drainage area along the channel length. The rationale for this can be seen by integrating equation (1), because the topographic gradient, S, is the derivative of elevation, z, with respect to downstream distance, x: i.e. $S = dz/dx$. Integration results in:

$$z(x) = z(x_b) + \left(\frac{k_s}{A_0{}^{\theta}}\right) \int_{x_b}^{x} \left(\frac{A_0}{A(x)}\right)^{\theta} dx \quad (2)$$

where A_0 is a reference drainage area, introduced to nondimensionalise the term within the integral, and x_b is the location of an arbitrary base level. Based on equation (2) we can define a longitudinal coordinate, χ, which has units of length (Royden et al., 2000; Perron and Royden, 2013):

$$\chi = \int_{x_b}^{x} \left(\frac{A_0}{A(x)}\right)^{\theta} dx \quad (3)$$

By defining χ in this way, equation (2) then reduces to:

$$z(x) = z(x_b) + \left(\frac{k_s}{A_0{}^{\theta}}\right) \chi. \quad (4)$$

Using equations (3) and (4) we can then calculate k_s (or more precisely k_{sn} because we must select a reference concavity index to perform the integration in equation 3) by regressing the local value of the gradient along the χ-elevation profile and normalizing for A_0. Parameter A_0 is selected to be 1 m^2 in order for k_s to correspond to the gradient k_{sn} in equation 4. This approach, called the integral method of channel analysis (or "chi" analysis) has been widely used in recent studies (e.g., Perron and Royden, 2013; Mudd et al., 2014; Mudd et al., 2018).

The values of the steepness index, k_{sn}, can adjust to changes in lithology, climate or rock uplift. We performed χ and k_{sn} analyses using the open-source algorithm from Mudd et al. (2014), using reference concavities (θ) of 0.45 calculated using the method of Mudd et al. (2018), in a range of catchments which cover a large part (about 80%) of the Pyrenees. Some high elevation portions of catchments present widespread geomorphic evidence of glacial erosion (Calvet, 2004) which are also associated with low k_{sn} values (Supplementary Figure 1) on glacial tributaries (e.g. MacGregor et al., 2000). For each catchment we define an elevation threshold that defines the altitude above which the majority of channels record evidence of glacial modification. Elevation threshold is defined by

extracting an elevation threshold where the majority of breaks exist in the χ versus elevation long profile and associated low k_{sn} values are observed (Supplementary Figure 1). Any k_{sn} measurements above this altitude are removed from the dataset (Supplementary Figure 2) in order to exclude channels profiles influenced by glacial erosion. However, this method can also potentially remove channel upper parts which are not influenced by glacial erosion. Complementary analyses are performed in order to test if varying reference concavities (i.e. 0.2 to 0.7) influence the relative magnitude of channel steepness (Supplementary Figure 3). We use SRTM data with a resolution of 30 m from the USGS EarthExplorer (http://earthexplorer.usgs.gov/) to perform the analyses (Fig. 2). Finally in order to compare the results of the topographic analyses with the effect of different lithologies we use a high resolution global lithological map (GLiM) (Hartmann and Moosdorf, 2012) (Fig. 2A). The GLiM dataset divides the Pyrenean geology into the following lithologies: unconsolidated sediments, siliciclastic sedimentary rocks, mixed sedimentary rocks, carbonate sedimentary rocks, metamorphic rocks, acid plutonic rocks, intermediate plutonic rocks, basic plutonic rocks, acid volcanic rocks, basic volcanic rocks and water bodies (Fig. 3C and D). In order to simplify the lithological data, we combine the three plutonic lithologies (acid, plutonic, intermediate) into the single category of 'plutonic rock'. The acid and basic volcanic rocks and water bodies are removed from the analyses as they are not sufficiently represented compared to the other lithologies.

We also analyse the drainage divide of the Pyrenees in order to compare its position relative to the distribution of lithologies. We focus this analysis on the influence of plutonic massifs on the location of the main drainage divide that separates north- from south-flowing rivers. For this we compare the proportion of the drainage divide that intersects the plutonic massifs against random lines parallel to the range. Forty hypothetical drainage divides parallel to the range front and intersecting the plutonic massif were taken. Hypothetical drainage divides are uniformly distributed in a box that covers the Pyrenees and encompassing all plutonic massifs (Figure 5). We then analyse the sinuosity index and the maximum lateral fluctuation of the main drainage divide from the Pyrenees and Western European Alps compared to active mountain ranges of Taiwan and Southern Alps of New Zealand. The sinuosity index corresponds to the ratio between the curvilinear length and the distance between the two extreme points of the drainage divide track. The maximum lateral fluctuation corresponds to the maximum

perpendicular distance of the drainage divide from a hypothetical straight line going through the two extreme points of the drainage divide.

3.2. Rock strength

In order to characterize the physical properties of each lithology we use the uniaxial compressive strength as a proxy for rock erodibility and approximate the durability of a rock to abrasion. Measurements of uniaxial compressive strength are carried out with a Schmidt hammer. The Schmidt hammer records the rebound velocity of a plunger that strikes the rock surface. Schmidt hammer measurements gained momentum in the 1960s and have been used in geomorphological research such as environmental controls of rock weathering. The Schmidt hammer uses a proprietary unit of compressive strength ranging from ~10 to ~100. The higher the rebound value, the higher the elastic strength of the rock.

Estimation of the uniaxial compressive strength from Schmidt hammers is susceptible to error because of the presence of fractures beneath the rock surface, moisture or local weathering at the surface of the rock. It is difficult to account for unseen fractures beneath the rock surface, but measurements are made at a minimum distance from visible fractures. Effects of surface weathering are mitigated by cleaning the rock surface and by performing several measurements on fresh fractured surfaces with no weathering. When dealing with metamorphic rocks characterized by foliation, rock compressive strength corresponds to the average of perpendicular and parallel measurements relative to the foliation. The suggested minimum sample size for Schmidt hammer dataset is 15 to 30 measurements on a single bedrock surface. We performed at least 30 measurements of bedrock surfaces at different locations for each different lithologies. The result is a compilation between 100 and 200 measurements for each of the main lithologies. Mean and median rebound values are then converted to compressive strength using conversion curves (determined from laboratory test) from manual of the Schmidt hammer model N used in the field.

3.3. Thermochronological approach

We performed new analyses of published thermochronological datasets from elevation profiles across a north-south transect in the Central Pyrenees (Fitzgerald et al., 1999; Sinclair et al., 2005; Gibson et al., 2007; Vacherat et al., 2016) (Supplementary Table 1 and 2 and Figure 2B and C). All available datasets are included in the analyses. Where there are multiple elevation profiles for the same massif, we chose the one with the largest number of samples and thermochronometric systems used. The aim was to resolve the timing of the last phase of deceleration in exhumation across the range. Elevation profiles are mainly located on Variscan crystalline basement massifs (exact location in figure 7 presented in the result section). The Nogueres profile is the southern-most profile and is situated on the Nogueres Zone (Sinclair et al., 2005, Gibson et al., 2007) which comprises Carboniferous volcanic rocks and has both apatite fission tracks (AFT) and zircon fission tracks (ZFT) data. Maladeta, Marimaña, Arties and Riberot profiles from south to north are located in the Axial Zone and correspond to high-relief Variscan granitoid massifs. The Maladeta and Marimaña massifs have apatite helium (AHe), AFT and ZFT data (Sinclair et al., 2005; Gibson et al., 2007) while Arties has AHe and AFT data (Gibson et al., 2007) and the Riberot profile only AFT data (Fitzgerald et al., 1999). The most northerly elevation profiles are the Trois-Seigneurs and Lacourt profiles corresponding also to granodioritic massifs and have AHe, AFT and ZFT data (Fitzgerald et al., 1999; Vacherat et al., 2016). The age ranges for AFT, AHe and ZFT, the mean track length for AFT system and the number of samples for each profiles are presented in Supplementary Tables 1 and 2.

In order to reconstruct accurate time-temperature histories we modelled the dataset using QTQt software (Gallagher, 2012), which inverts low-temperature thermochronological data. It uses the Bayesian Markov chain Monte Carlo methodology (Gallagher, 2012) and is specifically designed to model several samples from the same elevation profile. We use all samples in the profiles for modelling in order to take full advantage of the multi-sample inversion approach. This allows us to reduce the potential for both over interpretation and the introduction of artefacts in the inferred thermal histories (Gallagher et al., 2012). We use the latest kinetic model incorporated in the software with the multicompositional algorithms of Ketcham et al., (2007) for AFT and those of Yamada et al., (2007) for ZFT. For AHe we use the annealing and apatite radiation damage model of Gautheron et al. (2009).

To obtain robust thermal histories, at least 200,000 iterations are performed followed by a comparison between the observed data and the model predicted data (Supplementary Figure 4). The closure temperature of ZFT, AFT and AHe thermochronometers are unable to record post-orogenic events that occurred at temperatures below ~40 ºC. However, inverse modelling of this association of thermochronometer systems has the potential to record cooling deceleration for each thermal histories. The sensitivity of inverse modelling to accurately record deceleration is a function of model parameters (Gallagher et al., 2012; Gallagher, pers. comm.). The most influential parameters are: 1) the number and spatial coverage of samples along the vertical profiles; 2) the minimal elevation of the lower sample of the vertical profile; 3) the difference of cooling ages between the AFT and AHe system and its evolution along the vertical profile; 4) the distribution of apatite fission track lengths in samples along the vertical profile.

4. Results

4.1. Topographic and lithological analyses

Analyses of the k_{sn} parameter are first performed for each major catchment of the Pyrenean system (Supplementary Figure 5 and 6). In order to compare analyses of the different catchments we use a constant concavity index of 0.45, as this was the median concavity derived using the method of Mudd et al., (2018). Examples of the output are presented in Figure 3 from the Noguera Pallaresa catchment (Fig. 3A and C) located in the central southern Pyrenees, and the Garonne catchment (Fig. 3B and D) located in the central northern Pyrenees. Channel steepness is plotted as a succession of points every 30 m along river channels (Fig. 3A and B).

In order to quantify the impact of lithology on the landscape at the scale of an entire orogen we combine the results from the channel steepness analyses (Figs 3A and B and Supplementary Figure 7) from all of the non-glaciated catchments across the range (Fig. 2). Figure 4A highlights this result by showing a box and whisker plot of k_{sn} values associated with each of the main lithologies for the entire Pyrenees. The highest k_{sn} values are for the Variscan plutonic rocks with a mean and a median of 129

and 109 respectively. The metamorphic and mixed sedimentary rocks show notably lower mean and median k_{sn} compared to Variscan plutonic rocks with values of 116 and 105, and 113 and 100 respectively. The second important decrease of k_{sn} magnitude is observed with the carbonate and siliciclastic sedimentary rocks. Mean and median k_{sn} values are 74 and 53 respectively for the carbonate and 68 and 48 respectively for the siliciclastic rocks. The final break in k_{sn} magnitude corresponds to the unconsolidated sediment with a mean and median of 32 and 19 respectively.

4.2 Rock strength measurement

Results for the rebound value, *R*, show a variable pattern for the different lithologies (Fig. 4B). We convert the rebound value *R* to the rock compressive strength (MPa). Plutonic rocks record the maximum compressive strength with a mean value of 52 MPa. The rebound dataset of the plutonic rocks is also characterized by a quite narrow standard deviation of 8, which is due to the relative homogeneity of the plutonic rocks. Metamorphic and mixed sedimentary rocks are characterized by lower compressive strength values with a mean of 36 and 34 MPa respectively. Standard deviations of these two lithologies are also higher with a value of 11 MPa. These standard deviations highlight the heterogeneity in compressive strength of these two lithology group in which foliation and bedding play an important role. Carbonate and siliciclastic sedimentary rocks record a net rock strength reduction compared to the metamorphic and mixed sedimentary rocks. Mean rock compressive strengths are 26 and 24 MPa respectively for the carbonate sedimentary rocks and siliciclastic sedimentary rocks. Finally, the unconsolidated sedimentary rocks are characterized by a relatively low rock strength of 11 MPa.

4.3. Drainage divide analyses

The proportion of the main drainage divides located within plutonic massifs through the Pyrenees is presented in Figure 5. The mean percentage intersection for the forty hypothetical linear drainage divides is 15%. The percentage intersection for the actual modern drainage divide is 32%. The

analyses combined with a first order visual observation support a correlation between the position of the main drainage divide and the position of the plutonic massifs. Figure 6 shows results of the sinuosity index and maximum lateral fluctuation for the Pyrenees, Western Alps, Taiwan and New Zealand; Taiwan and New Zealand are considered as example of actively accreting mountain ranges, and the Western Alps as an example of a range that has had approximately 5 Myr of isostatic rebound and post-orogenic decay (based on the definition outlined in the Introduction). The sinuosity index for these ranges is 1.47, 1.72, 1.29 and 1.12. Maximum and mean lateral fluctuation are respectively 30.1 and 14.2±5.3 km for the Pyrenees, 43.9 and 23.62±9.14 km for the Western Alps, 18.4 and 7.36±3.52 km for Taiwan and 18.0 and 8.13±3.64 for New-Zealand. These result show that the Pyrenees and Western Alps are characterised by a drainage divide with a high degree of sinuosity compare to Taiwan and New Zealand (Fig. 6). Maximum lateral variations in the drainage divide differ also between the different ranges. Maximum lateral variation of the Pyrenees and Western Alps are almost twice as extensive as those observed for New Zealand or Taiwan (Fig. 6).

4.3. Thermal histories of the Central Pyrenees

Thermal histories are presented in Figures 7B-I for eight localities with elevation profiles in the Central Pyrenees (Fig. 7A). For each thermal history built using QTQt we compared the predicted data, generated by multiple modelled thermal histories, to the observed data (Supplementary Figure 4). From these data we map the best-fit cooling rate along a north-south transect (Fig. 8).

Figures 7 and 8 compare the time-temperature paths of each of the localities. The start of accelerated cooling is different for each elevation profile and youngs from north to south as has been reported previously (Fitzgerald et al., 1999; Sinclair et al., 2005). The time when cooling rates decreased varies from the different profiles with a systematic younging from north to south (supplementary Table 3). Deceleration of cooling is less evident for the Barruera profile but thermal histories appear to reach a constant cooling rate at about 7 Ma (Fig. 8C). The general pattern of cooling along the Central Pyrenees is characterized by a diachronous onset and termination of rapid cooling.

The time of the decrease in the cooling rate, i.e. the time from the start of the decrease, to the end of the change in cooling rate defined from the inflexion point on the curve (Fig. 8C), is variable between profiles (Supplementary Table 3). It corresponds to the time when the cooling rate goes from high values (yellow-red colours in figure 8) to stable values (blue colours in Figure 8). By dividing the change of cooling rate during deceleration with the corresponding duration of deceleration, the rate of change of cooling (Supplementary Table 3) is revealed. The profiles located at the northern and southern edges of the mountain range (Lacourt, Barruera and Nogueres) record a slow deceleration in cooling rate. In contrast, profiles situated in the core of the mountain range such as Maladeta, Arties, Marimaña and Riberot record relatively rapid decelerations.

5. Discussion

5.1. Lithological effect on river profiles

The topographic analyses for the entire Pyrenean orogen reveals a correlation between the channel steepness index (k_{sn}) and rock compressive strength associated with each lithology (Fig. 4). Plutonic rocks are characterised by higher channel steepness and high rock compressive strength (Fig. 4A and B). The metamorphic and mixed sedimentary rocks are associated with lower channel steepness and rock compressive strength compared to plutonic rocks. Finally, the two parameters are lower again for carbonate and siliciclastic sedimentary rocks. Figure 4C shows the direct correlation of the mean (correlation coefficient of 0.95) and median (correlation coefficient of 0.93) values between channel steepness and rock strength associated to each lithology. For both cases, there is a linear relationship between these two parameters indicating correlation between lithology, channel steepness and rock compressive strength. Elevation and lithology distribution seem also to be closely correlated. Swath profiles (Figure 9A, B and C) of the western, center and eastern Pyrenees (Figure 1) combined with a regional correlation between elevation and lithology (Figure 9D) indicate that plutonic and metamorphic rocks (high rock strength) consistently occupy the regions of higher elevation relative to the other lithologies.

Plucking during river erosion of mountain ranges is modulated mainly by the occurrence of joints, fractures and bedding (Whipple et al., 2000). Plutonic rocks tend to have the lowest density of fractures or joints compared to other rock types and are thus potentially more resistant to plucking (Whipple et al., 2000). Variation in rock strengths and especially high rock strength for the plutonic range are consistent with fracture and joint expectations.

The principal modern agent of erosion in the Pyrenees is fluvial erosion, although there is extensive evidence of glacial impact on channel profiles within the Pyrenees (Calvet, 2004). Glacial erosion tends to increase hillslope steepness by forming ridges and arêtes in the high-elevation part of the mountain and have the potential to lower channel gradients and their concavities (MacGregor et al., 2000; Brocklehurst and Whipple, 2002). Therefore, we would expect glacial erosion to have reduced channel gradients in the centre of the Pyrenean orogeny, which is where the harder plutonic and metamorphic rocks are mostly located (Figure 2A). Glaciation could then potentially impact the correlation between rock strength of different lithologies and channel steepness (Figure 4, Supplementary Figure 1 and 2). The mean altitude of the transition from fluvial to glacially-dominated long profiles varies between catchments. The transition for the Noguera Pallaresa (Supplementary Figure 2) ranges between 1900 and 2100 m. Transitions from different catchments seem to indicate a generally higher elevation for the southern basins compared to northern basins and can results from the more arid southern Pyrenees relatively to the northern side. The exclusion of k_{sn} values at elevations above the transition has an impact on the correlation between lithology and channel steepness with a general increase of the mean k_{sn} values for plutonic lithologies (Supplementary Figure 2A and B). Orographic enhancement of precipitation with greater precipitation in the northern Pyrenees than the south may result in increased discharge per unit area of catchment, and hence may lead to a decrease in k_{sn} from south to north, and may influence the degree of glacial impact. However, there is no evidence to suggest a significant difference in k_{sn} values between the northern and southern portions of the Pyrenees (Supplementary Figure 5, 6 and 7).

Other external forces such as spatially varying uplift rates induced by tectonic activity can impact channel steepness, however, given the ca. 20 Myrs since significant fault induced changes in exhumation rates, it is not considered a significant factor in the current case. Only the thermal history

395 from the Barruera profile shows limited cooling that is associated to the late activity of the antiformal
396 stack (Sinclair et al., 2005). Surface uplift of the eastern Pyrenees since middle Miocene times has been
397 proposed related to opening of the Gulf of Lyon further East (Calvet and Gunnel, 2008) and could have
398 caused recent differential uplift in the eastern side of the range. However, we don't observe any notable
399 difference in the range of k_{sn} values for the eastern catchments compare to others (Supplementary Figure
400 5 and 6).
401
402 *5.2 Effect of lithology on the drainage divide*
403
404 In a doubly-vergent mountain range such as the Pyrenees or Southern Alps of New Zealand,
405 the main drainage divide provides a robust first order dividing line between the pro- and retro-sides of
406 the mountain system. General evolutionary models coupling tectonics and surface processes indicate
407 the development of a generally straight drainage divide roughly parallel with the mountain front and
408 tracking the thickest part of a doubly-vergent wedge located above the S-point (Koons, 1989). The
409 exact location of the drainage divide during orogenesis fluctuates according to the relative proportions
410 of frontal accretion and underplating (Willett et al., 2001) and is generally pushed toward the retro-side
411 of the orogen. Tectonics play an important role in determining the position of the drainage divide but
412 studies show that the climate can also alter this position, either by enhancing or acting against the
413 tectonic signal (Koons, 1989; Willet et al., 1999).
414 The Pyrenees comprise an Axial Zone characterised by several Variscan granitoid massifs. (Fig.
415 1 and 5) surrounded by sedimentary and low-grade metamorphic rocks. From a first visual observation,
416 the drainage divide appears to approximately track the location of the plutonic massifs (Fig. 5).
417 Furthermore, the mean percentage of intersections with plutonic rocks from random linear lines (15%)
418 is significantly lower than the one from the actual drainage divide (32%). The results suggest that
419 plutonic massifs influence the current position of the Pyrenean drainage divide. The Pyrenees and
420 Western European Alps present more irregular drainage divides relative to the Southern Alps of New
421 Zealand and Taiwan which are similar in size to the Pyrenees, but are actively shortening (Figure 6).
422 These active systems are characterized by relatively linear drainage divides with minor lateral

423 fluctuation that split the pro- from the retro-wedges of the range indicating that they are primarily
424 controlled by the advection of rock within the active doubly-vergent thrust wedges (Willett et al., 2001;
425 Fig. 6). The implication being that the switch from syn- to post-orogenic topography is characterised
426 by a modification of the drainage divide, which becomes more strongly determined by rock strength as
427 tectonic advection of rock ceases.
428
429 *5.3. Thermochronologic data and variation of rock type exposed through time*
430
431 Changes in rates of rock exhumation in active mountain ranges are often interpreted in terms
432 of the punctuated forcing of by thrust activity (e.g. Naylor and Sinclair, 2007) or changes in the erosive
433 capacity of the climate (e.g. Thiede et al., 2004). The timing of deceleration in cooling rates (Figure 8)
434 demonstrates that the transition from rapid to slow exhumation rates is diachronous from north to south
435 across the Pyrenean mountain belt. The diachroneity in the decrease in exhumation rate can be explained
436 by the diachronous termination of structural activity in the Axial Zone as predicted in modelling of
437 active thrust wedges (Naylor and Sinclair, 2007; Gibson et al., 2008).
438 Modelling results of Flowers and Ehlers (2018) suggest that even relatively low contrasts in the
439 erodibility of bedrock (by factors of between two and ten) can influence thermal histories if the rock
440 layers are relatively thick ($\geq$ 2 km) and the cumulative erosion magnitude is relatively high (at least 4
441 km for AHe data and 6-8 km for AFT data). These results suggest that in the geological scenario of a
442 sedimentary cover overlying crystalline basement rock (i.e. Mesozoic and Palaeozoic cover of the
443 Variscan Massifs in the Pyrenees), the reduction in exhumation rates due to lithology changes at the
444 surface should be recorded in the thermochronometric ages; this is also suggested for the Tien Shan
445 (Sobel et al., 2006) and the Western European Alps (Glotzbach et al., 2011). In the Pyrenees, with the
446 exception of the Nogueres profile, thermal histories have been modelled from the Variscan crystalline
447 basement massifs. These massifs were overlain by a succession of Upper Paleozoic and Mesozoic
448 sedimentary strata according to structural reconstructions (e.g. Muñoz, 1992; Beaumont et al., 2000).
449 The measured rock strengths in the granitoid massifs are 1.5 to 2 times higher than the surrounding and
450 originally overlying successions. If fracture density and structural heterogeneities are also considered

451 in evaluating bulk rock strength then the contrast between the erodibility of the granitoid basement and
452 the Upper Paleozoic and Mesozoic sedimentary successions would likely be even greater. Therefore, it
453 would be expected that there be some record of reduced exhumation rates in response to erosion through
454 the sedimentary successions into the Variscan granitoid basement. Results from the thermal histories
455 modelling (Fig. 7) are consistent with this hypothesis. Indeed, thermal histories from Maladeta, Arties,
456 Marimaña and Riberot characterised by large Variscan plutons and surrounded by Silurian to Cambrian
457 meta-sedimentary rocks show a strong deceleration of the cooling (Fig. 7A and 7B). In contrast, thermal
458 histories from Nogueres, Barruera, Trois-Seigneurs or Lacourt record a gentler deceleration. However,
459 the abrupt deceleration of some of the southern massifs may also be attributed to valley backfilling
460 during the endorheic stage in the southern Ebro basin (Convey et al., 1996).

461 Evidence for the emergence of basement rocks during orogenesis may be recorded in the
462 sedimentological record. Syn-tectonic sediment is well preserved in the South Pyrenean Thrust Belt
463 where Mesozoic carbonates are overlain by syn-tectonic Paleogene siliciclastic sandstones and
464 conglomerates (Vergès and Muñoz, 1990; Meigs et al., 1996). The Sis palaeovalley records long-term
465 conglomerate accumulation and demonstrates that granitoid clasts were first present in small quantities
466 (<12%) in early Ypresian times (ca. 54.5 Ma) until at least Rupelian/early Chattian times (ca. 27.8 Ma;
467 Vincent, 2001). Granitic clasts make up about 4% of the mid-late Eocene Escanilla system of the central
468 southern Pyrenees (Michael et al., 2014). The late Eocene and Oligocene conglomerates around Poble
469 de Segur are dominated by red Permian and Triassic sandstones and Palaeozoic metasedimentary rocks,
470 with few clasts of granitoid lithologies (Mellere, 2009). The early Eocene to late Oligocene Carcassone
471 Group of the proximal Aquitaine Basin comprises a series of conglomerates with occasional granitoid
472 clasts. The presence of granitoid clasts in the syn-tectonic sedimentary successions of the Pyrenees
473 demonstrates that the Variscan Massifs were being exposed throughout the evolution of the range from
474 mid-Eocene onward. We conclude that the contrast in rock strength between the sedimentary cover and
475 crystalline basement in the Pyrenees must be viewed as a probable control on the history of erosion and
476 exhumation of the range.

477

478 **6. Conclusion**

The post-orogenic topography of the Pyrenees is influenced by varying rock strength of the main lithological units, and we suggest this also impacted the syn-orogenic exhumation of the range. We quantify rock strength using elastic rebound measurements recorded using a Schmidt hammer, and demonstrate that the granitoid lithologies of the Variscan massifs have the greatest strength, with Palaeozoic metasediments, Mesozoic and Tertiary cover rocks recording progressively weaker lithologies. The strength of rock is also revealed by measurements of the steepness of river channels normalised to the upstream area; high, normalised channel steepness indices broadly correlate with areas of high rock strength across the range. The highest rock strengths also correlate to the highest elevation topography, with the main drainage divide preferentially tracking the Variscan granitoid massifs of the Axial Zone forming the spine of the range. By comparing the geometry of the drainage divide of the post-orogenic Pyrenees to similar-sized, tectonically active ranges, we suggest that, in the recent evolution of the Pyrenees, lithology plays a more dominant role than tectonics. Thermal modelling of thermochronological datasets from the Central Pyrenees reveal a southward migration and abrupt decelerations in cooling/erosion histories in granitic massifs; we suggest that exhumation of crystalline basement following removal of overlying sedimentary cover is also likely to have influenced the syn-tectonic erosional history of the syn-tectonic history of the range.

Author contributions: All authors participated to the writing of the text according to the following order of contribution: T.B., H.D.S., S.M.M., M.F. and B.G.. T.B., B.G. and S.M. performed the topographic numerical modelling. T.B. performed the inverse modelling of the low-temperature thermochronological dataset. T.B. performed the Schmidt Hammer measurements on the field. M.F. and H.D.S. initiated the project.

Competing interests: The authors declare that they have no conflict of interest.

Acknowledgements: We thank Pierre Valla and Peter van der Beek for constructive comments which allowed us to improve the paper quality. We thank Jean-Philippe Avouac for editorial guidance.

Funding: This study was supported by the OROGEN project, a TOTAL-BRGM-CNRS consortium.

BIBLIOGRAPHY:

Baldwin, J.A., Whipple, K.X., Tucker, G.E., 2003. Implications of the shear stress river incision model for the timescale of postorogenic decay of topography. J. Geophys. Res. Solid Earth. https://doi.org/10.1029/2001JB000550

Beaumont, C., Muñoz, J.A., Hamilton, J., Fullsack, P., 2000. Factors controlling the Alpine evolution of the central Pyrenees inferred from a comparison of observations and geodynamical models. J. Geophys. Res. Solid Earth. https://doi.org/10.1029/1999JB900390

Beaumont, C., Jamieson, R.A., Nguyen, M.H., Lee, B., 2001. Himalayan tectonics explained by extrusion of a low-viscosity crustal channel coupled to focused surface denudation. Nature. https://doi.org/10.1038/414738a

Bourrouilh, R., Richert, J.P., Zolnai, G., 1995. The north Pyrenean Aquitaine Basin, France: evolution and hydrocarbons. Am. Assoc. Pet. Geol. Bull. https://doi.org/10.1306/8D2B1BC4-171E-11D7-8645000102C1865D

Brocklehurst, S.H., Whipple, K.X., 2002. Glacial erosion and relief production in the Eastern Sierra Nevada, California. Geomorphology. https://doi.org/10.1016/S0169-555X(01)00069-1

Brunet, M.F., 1986. The influence of the evolution of the Pyrenees on adjacent basins. Tectonophysics. https://doi.org/10.1016/0040-1951(86)90260-X

Calvet, M., 2004. The Quaternary glaciation of the Pyrenees. Dev. Quat. Sci. https://doi.org/10.1016/S1571-0866(04)80062-9

Calvet, M., Gunnell, Y., 2008. Planar landforms as markers of denudation chronology: an inversion of East Pyrenean tectonics based on landscape and sedimentary basin analysis. Geol. Soc. London, Spec. Publ. https://doi.org/10.1144/SP296.10

Fillon, C., Gautheron, C., van der Beek, P., 2013. Oligocene–Miocene burial and exhumation of the Southern Pyrenean foreland quantified by low-temperature thermochronology. J. Geol. Soc. London. https://doi.org/10.1144/jgs2012-051

Fitzgerald, P.G., Muñoz, J.A., Coney, P.J., Baldwin, S.L., 1999. Asymmetric exhumation across the Pyrenean orogen: Implications for the tectonic evolution of a collisional orogen. Earth Planet. Sci. Lett. https://doi.org/10.1016/S0012-821X(99)00225-3

Flowers, R.M., Ehlers, T.A., 2018. Rock erodibility and the interpretation of low-temperature thermochronologic data. Earth Planet. Sci. Lett. https://doi.org/10.1016/j.epsl.2017.11.018

Gallagher, K., 2012. Transdimensional inverse thermal history modeling for quantitative thermochronology. J. Geophys. Res. Solid Earth. https://doi.org/10.1029/2011JB008825

Gautheron, C., Tassan-Got, L., Barbarand, J., Pagel, M., 2009. Effect of alpha-damage annealing on apatite (U-Th)/He thermochronology. Chem. Geol. https://doi.org/10.1016/j.chemgeo.2009.06.001

Gibson, M., Sinclair, H.D., Lynn, G.J., Stuart, F.M., 2007. Late- to post-orogenic exhumation of the central Pyrenees revealed through combined thermochronological data and modelling. Basin Res. https://doi.org/10.1111/j.1365-2117.2007.00333.x

Gilbert, G.K., 1877. Land Sculptures - Geology of the Henry Mountains. Monograph. https://doi.org/10.1038/022266c0

Glotzbach, C., van der Beek, P.A., Spiegel, C., 2011. Episodic exhumation and relief growth in the Mont Blanc massif, Western Alps from numerical modelling of thermochronology data. Earth Planet. Sci. Lett. https://doi.org/10.1016/j.epsl.2011.02.020

Harel, M.-A., Mudd, S.M., Attal, M., 2016. Global analysis of the stream power law parameters based on worldwide 10Be denudation rates. Geomorphology 268, 184–196. https://doi.org/10.1016/j.geomorph.2016.05.035

Hartmann, J., Moosdorf, N., 2012. The new global lithological map database GLiM: A representation of rock properties at the Earth surface. Geochemistry, Geophys. Geosystems. https://doi.org/10.1029/2012GC004370

Jolivet, M., Labaume, P., Monié, P., Brunel, M., Arnaud, N., Campani, M., 2007. Thermochronology constraints for the propagation sequence of the south Pyrenean basement thrust system (France-Spain). Tectonics. https://doi.org/10.1029/2006TC002080

Ketcham, R.A., Carter, A., Donelick, R.A., Barbarand, J., Hurford, A.J., 2007. Improved modeling of fission-track annealing in apatite. Am. Mineral. https://doi.org/10.2138/am.2007.2281

Koons, P.O., 1990. Two-sided orogen: collision and erosion from the sandbox to the Southern Alps, New Zealand. Geology. https://doi.org/10.1130/0091-7613(1990)018<0679:TSOCAE>2.3.CO;2

Koons, P.O., Upton, P., Barker, A.D., 2012. The influence of mechanical properties on the link between tectonic and topographic evolution. Geomorphology. https://doi.org/10.1016/j.geomorph.2010.11.012

Lynn, G.J., 2005. Macrogeomorphology and erosional history of the postorogenic Pyrenean mountain belt. PhD Thesis, University of Edinburgh.

MacGregor, K.R., Anderson, R.S., Anderson, S.P., Waddington, E.D., 2000. Numerical simulations of glacial-valley longitudinal profile evolution. Geology. https://doi.org/10.1130/0091-7613(2000)028<1031:NSOGVL>2.3.CO;2

Matenco, L., 2017. Tectonics and exhumation of Romanian carpathians: Inferences from kinematic and thermochronological studies, in: Springer Geography. https://doi.org/10.1007/978-3-319-32589-7_2

Meigs, A.J., Vergés, J., Burbank, D.W., 1996. Ten-million-year history of a thrust sheet. Bull. Geol. Soc. Am. https://doi.org/10.1130/0016-7606(1996)108<1608:TMYHOA>2.3.CO;2

Mellere, D., 2009. Thrust-Generated, Back-Fill Stacking of Alluvial Fan Sequences, South-Central Pyrenees, Spain (La Pobla De Segur Conglomerates), in: Tectonic Controls and Signatures in Sedimentary Successions. https://doi.org/10.1002/9781444304053.ch14

Morisawa, M.E., 1962. Quantitative Geomorphology of Some Watersheds in the Appalachian Plateau. GSA Bulletin 73, 1025–1046. https://doi.org/10.1130/0016-7606(1962)73[1025:QGOSWI]2.0.CO;2

Mudd, S.M., Attal, M., Milodowski, D.T., Grieve, S.W.D., Valters, D.A., 2014. A statistical framework to quantify spatial variation in channel gradients using the integral method of channel profile analysis. J. Geophys. Res. Earth Surf. https://doi.org/10.1002/2013JF002981

Mudd, S.M., Clubb, F.J., Gailleton, B., Hurst, M.D., 2018. How concave are river channels? Earth Surface Dynamics 6, 505–523. https://doi.org/10.5194/esurf-6-505-2018

Muñoz, J.A., 1992. Evolution of a continental collision belt: ECORS-Pyrenees crustal balanced cross-section, in: Thrust Tectonics. https://doi.org/10.1007/978-94-011-3066-0_21

Naylor, M., Sinclair, H.D., 2007. Punctuated thrust deformation in the context of doubly vergent thrust wedges: Implications for the location of uplift and exhumation. Geology. https://doi.org/10.1130/G23448A.1

Perron, J.T., Royden, L., 2013. An integral approach to bedrock river profile analysis. Earth Surf. Process. Landforms. https://doi.org/10.1002/esp.3302

Roest, W.R., Srivastava, S.P., 1991. Kinematics of the plate boundaries between Eurasia, Iberia, and Africa in the North Atlantic from the Late Cretaceous to the present. Geology. https://doi.org/10.1130/0091-7613(1991)019<0613:KOTPBB>2.3.CO;2

Scharf, T.E., Codilean, A.T., De Wit, M., Jansen, J.D., Kubik, P.W., 2013. Strong rocks sustain ancient postorogenic topography in southern Africa. Geology. https://doi.org/10.1130/G33806.1

Sinclair, H.D., Gibson, M., Naylor, M., Morris, R.G., 2005. Asymmetric growth of the Pyrenees revealed through measurement and modeling of orogenic fluxes. Am. J. Sci. https://doi.org/10.2475/ajs.305.5.369

Sklar, L.S., Dietrich, W.E., 2001. Sediment and rock strength controls on river incision into bedrock. Geology. https://doi.org/10.1130/0091-7613(2001)029<1087:SARSCO>2.0.CO

Sobel, E.R., Chen, J., Heermance, R. V., 2006. Late Oligocene-Early Miocene initiation of shortening in the Southwestern Chinese Tian Shan: Implications for Neogene shortening rate variations. Earth Planet. Sci. Lett. https://doi.org/10.1016/j.epsl.2006.03.048

Thiede, R.C., Bookhagen, B., Arrowsmith, J.R., Sobel, E.R., Strecker, M.R., 2004. Climatic control on rapid exhumation along the Southern Himalayan Front. Earth Planet. Sci. Lett. https://doi.org/10.1016/j.epsl.2004.03.015

Tucker, G.E., van der Beek, P., 2013. A model for post-orogenic development of a mountain range and its foreland. Basin Res. https://doi.org/10.1111/j.1365-2117.2012.00559.x

Vacherat, A., Mouthereau, F., Pik, R., Bellahsen, N., Gautheron, C., Bernet, M., Daudet, M., Balansa, J., Tibari, B., Pinna Jamme, R., Radal, J., 2016. Rift-to-collision transition recorded by tectonothermal evolution of the northern Pyrenees. Tectonics. https://doi.org/10.1002/2015TC004016

Valla, P.G., Van Der Beek, P.A., Shuster, D.L., Braun, J., Herman, F., Tassan-Got, L., Gautheron, C., 2012. Late Neogene exhumation and relief development of the Aar and Aiguilles Rouges massifs (Swiss Alps) from low-temperature thermochronology modeling and 4He/3He thermochronometry. J. Geophys. Res. Earth Surf. https://doi.org/10.1029/2011JF002043

Verges, J., Munoz, J.A., 1990. Thrust sequences in the southern central {Pyrenees}. Bull. la Société Géologique Fr. https://doi.org/10.2113/gssgfbull.VI.2.265

Vincent, S.J., 2001. The Sis palaeovalley: A record of proximal fluvial sedimentation and drainage basin development in response to Pyrenean mountain building. Sedimentology. https://doi.org/10.1046/j.1365-3091.2001.00421.x

Whipple, K.X., Hancock, G.S., Anderson, R.S., 2000. River incision into bedrock: Mechanics and relative efficacy of plucking, abrasion, and cavitation. Bull. Geol. Soc. Am. https://doi.org/10.1130/0016-7606(2000)112<490:RIIBMA>2.0.CO;2

Willett, S.D., 1999. Orogeny and orography: The effects of erosion on the structure of mountain belts. J. Geophys. Res. Solid Earth. https://doi.org/10.1029/1999JB900248

Willett, S.D., Slingerland, R., Hovius, N., 2001. Uplift, shortening, and steady state topography in active mountain belts. Am. J. Sci. https://doi.org/10.2475/ajs.301.4-5.455

Wobus, C., Whipple, K.X., Kirby, E., Snyder, N., Johnson, J., Spyropolou, K., Crosby, B., Sheehan, D., 2006. Tectonics from topography: Procedures, promise, and pitfalls, in: Special Paper 398: Tectonics, Climate, and Landscape Evolution. https://doi.org/10.1130/2006.2398(04)

Yamada, R., Murakami, M., Tagami, T., 2007. Statistical modelling of annealing kinetics of fission tracks in zircon; Reassessment of laboratory experiments. Chem. Geol. https://doi.org/10.1016/j.chemgeo.2006.09.002

Yelland, A.J., 1990. Fission track thermotectonics in the Pyrenean orogen. Int. J. Radiat. Appl. Instrumentation. Part. https://doi.org/10.1016/1359-0189(90)90049-4

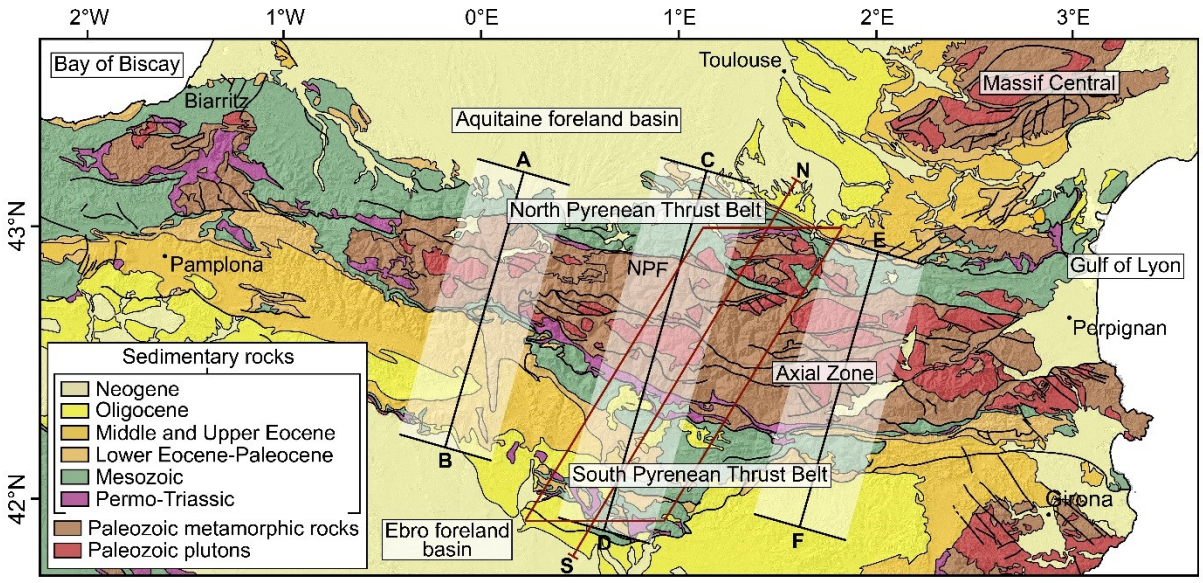

Figure 1 (2-columns, color): Geologic map of the Pyrenees from the 1:1000000 BRGM geological map of France draped on a hillslope map from a SRTM with a resolution of 30 m. Red rectangle highlights the area of figure 7 and the red line indicates the approximate position of the geologic cross-section in Figure 4B. NPF: North Pyrenean Fault. Black lines and white transparent areas indicate locations of the different swath profiles of supplementary figure 9. Cities are indicated by black dots.

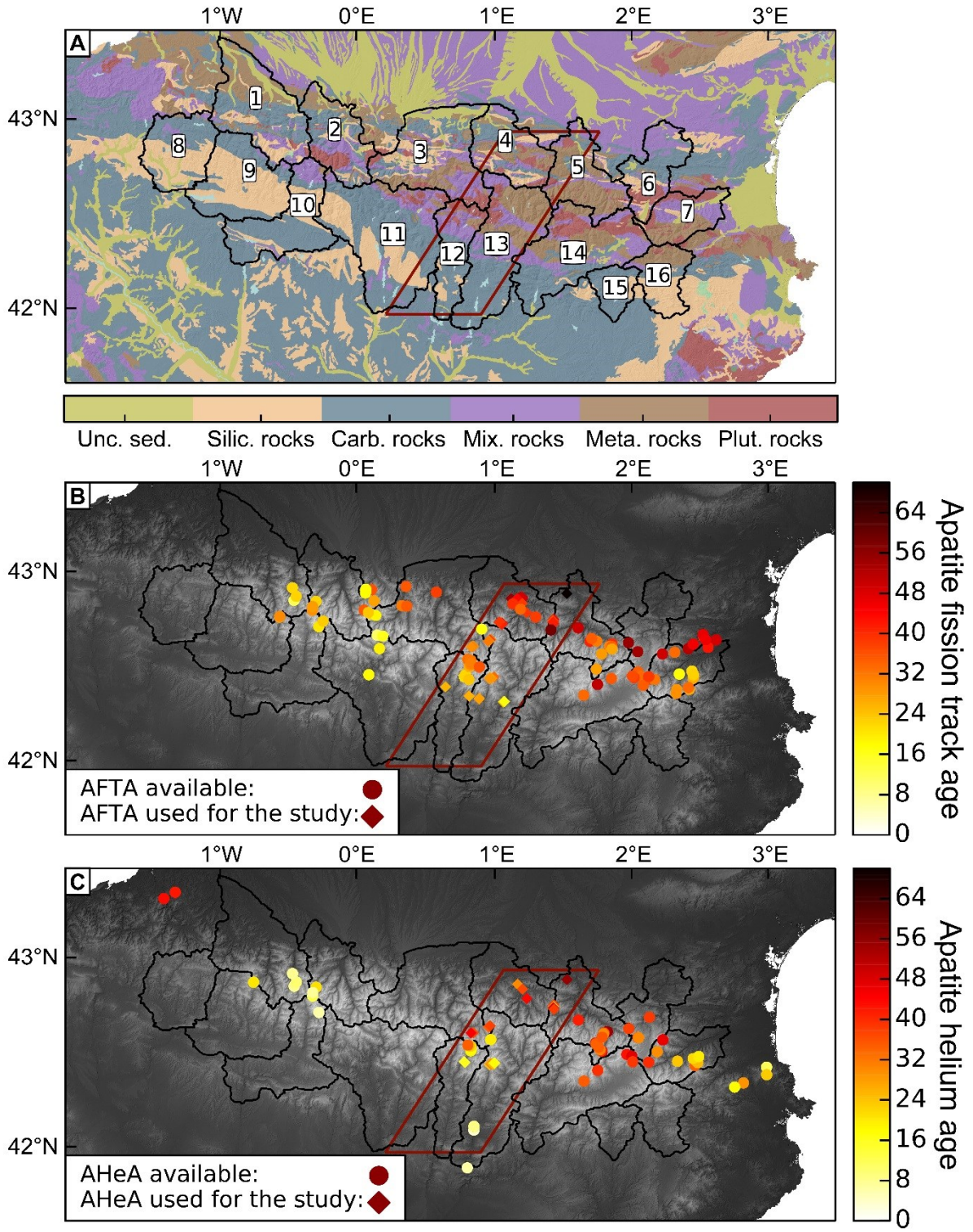

Figure 2 (2-columns, color): Maps of the Pyrenean drainage system from SRTM data with a resolution of 30 m. Black outlines represent the main catchments and the red line corresponds to the area in the Figure 7. A) Lithologic map of the Pyrenean system from the high resolution global geological map GLiM (Hartmann and Moosdorf, 2012) (Unc. Sed.: unconsolidated sediments; Silic. rocks: siliciclastic sedimentary rocks; Carb. rocks: carbonate sedimentary rocks; Mix. rocks: mixed sedimentary rocks; Meta. rocks: metamorphic rocks; Plut. rocks: plutonic rocks). The different catchments are labelled on the map as follows: (1) Saison, (2) Gave de Pau, (3) Garonne, (4) Salat, (5) Ariège, (6) Aude, (7) Tet, (8) Irati, (9) Aragon, (10) Gallego, (11) Cinca, (12) Noguera Ribagorzana, (13) Noguera Pallaresa, (14)

Segre, (15) Llobegrat and (16) Ter. Garonne (3) and Noguera Pallaresa (13) catchments are used as examples in Figure 3. B) Black and white topographic map of the study area with a compilation of apatite fission track ages represented by circles of white-yellow to red-black colors depending on age. Apatite fission track ages used in this study are represented with diamonds. C) Black and white topographic map of Pyrenees with a compilation of apatite helium ages in the Pyrenees represented by circle shape of white-yellow to red-black colors depending of the age. Apatite-helium ages used in this study are represented with diamonds (source of data are provided in supplementary tables 1 and 2).

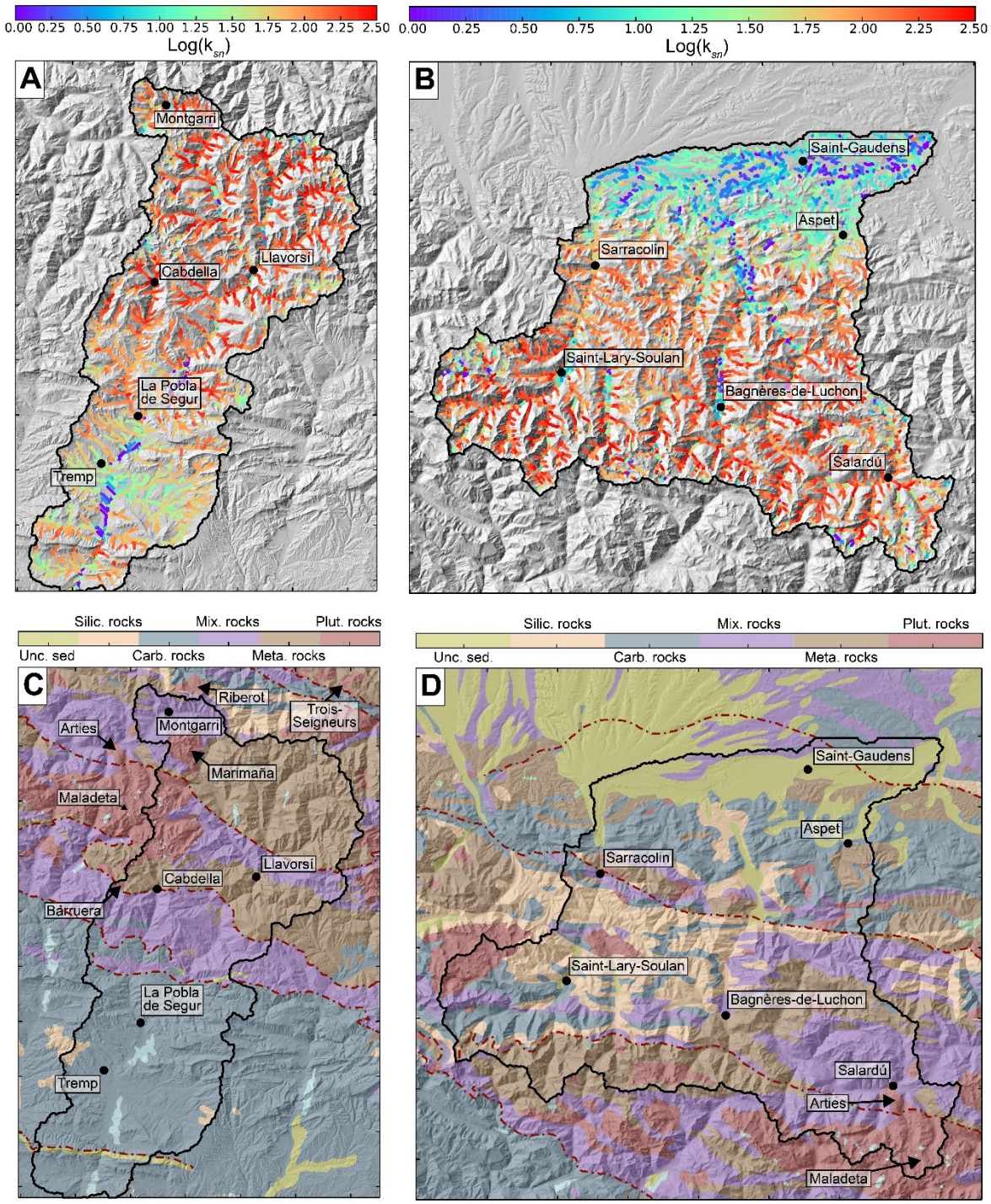

Figure 3 (2-columns, color): Relation between topography, lithology and k_{sn} in two catchment examples. Top panels are maps of k_{sn} for A) the Noguera Pallaresa catchment (south side prowedge) and B) the Garonne catchment (north side retrowedge). The Log(k_{sn}) parameter is represented by a succession of points along the river channel of the catchment with bright colors from purple (low values) to red (high value). The legend for the k_{sn} parameter is plotted above the panels. Lower panels (C and D) correspond to the same areas but with the lithology represented in colors. The legend of lithology is plotted above the panels and corresponds with lithology colors in Figure 1A. Cities are represented by black dots and massifs by black arrows. Red dash lines correspond to the main faults.

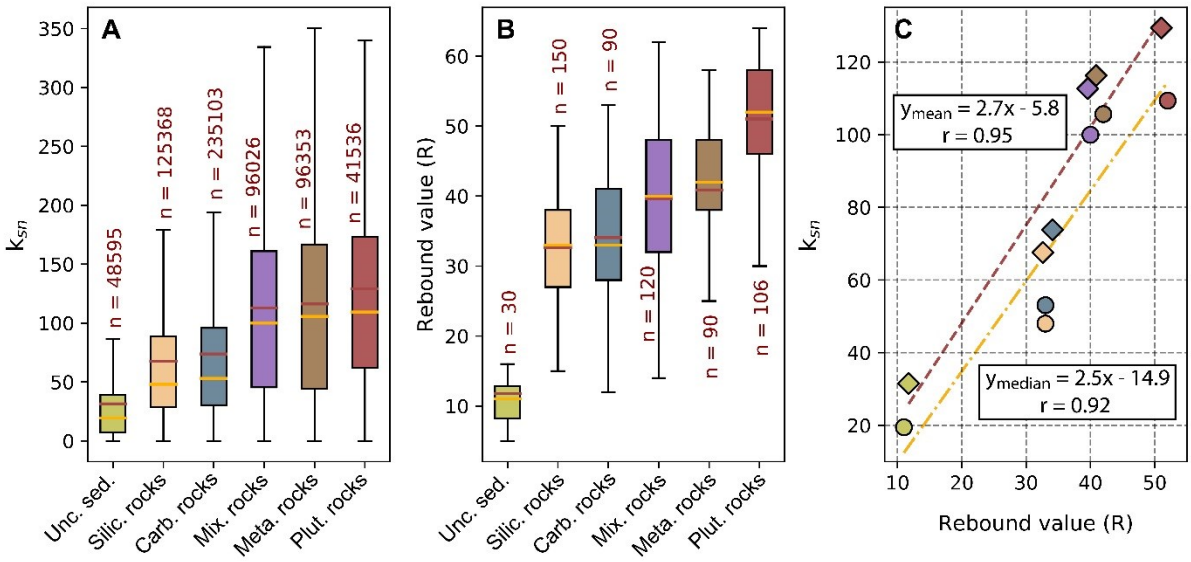

Figure 4 (2-columns, color): Channel steepness, rock strength and lithology correlations. Whisker and boxplot representation of A) k_{sn} and B) rebound value (R) plotted as a function of lithology. The number of values analysed associated to each lithology is displayed in red above or under the boxplot. Colors of boxplots and lithology abbreviations are in accord with figure 2. Each box-and-whisker, in this figure, represents the minimal, 25th percentiles, 75th percentiles and maximal values in horizontal black lines while red and yellow horizontal lines represent respectively the mean and median values. C) Correlation between mean values (diamonds and red normal dashed line) and median values (rounds and yellow point dashed lines) of the channel steepness and rock strength. r is the correlation coefficient.

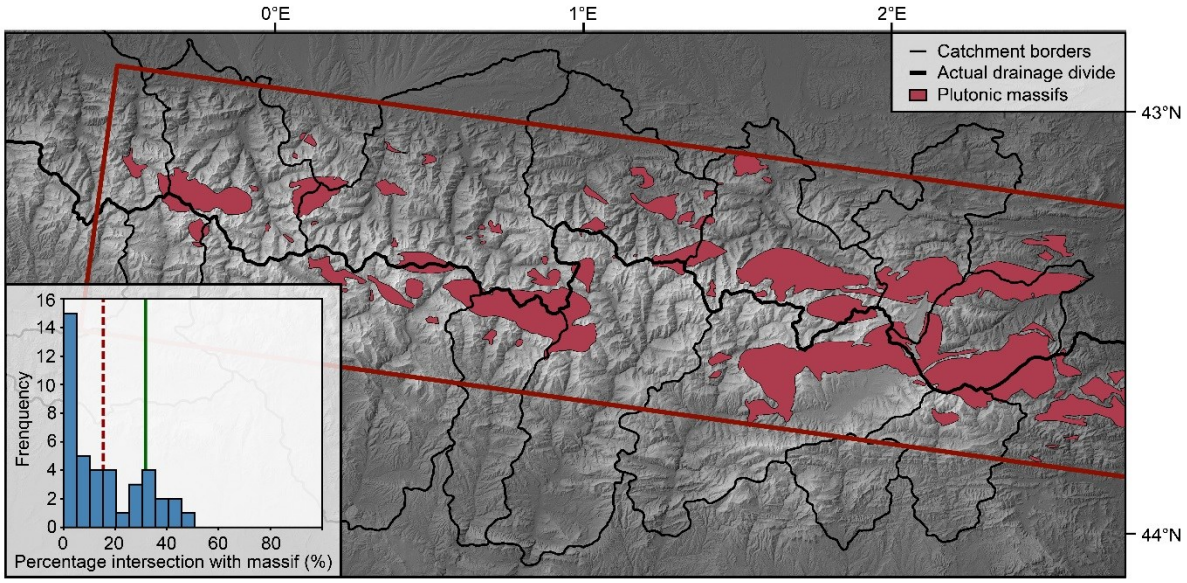

Figure 5 (2-columns, color): Topographic map of the Pyrenees from SRTM with a resolution of 30 m. The different Variscan plutonic massifs are plotted in red. The main and secondary drainage divide (associated to the delimitation of catchments) are represented respectively with a thick black line and with thin black lines (Based on Lynn, 2005). Frequency of the percentage intersection for random drainage with plutonic massifs is plotted in the lower left side. Forty hypothetical drainage divided parallel to the range have been analysed. For each linear drainage divide, the proportion of the line that intersected the plutonic massifs was calculated as a percentage. The mean percentage intersection with plutonic massifs from the forty hypothetical drainage divides is compared to the percentage intersection of the main drainage divide. The dashed vertical red line on the graph corresponds to the mean percentage of intersection of the random linear lines. The vertical green line corresponds to the percentage intersection of the modern drainage divide. The red box shows the area of the forty hypothetical drainage divides.

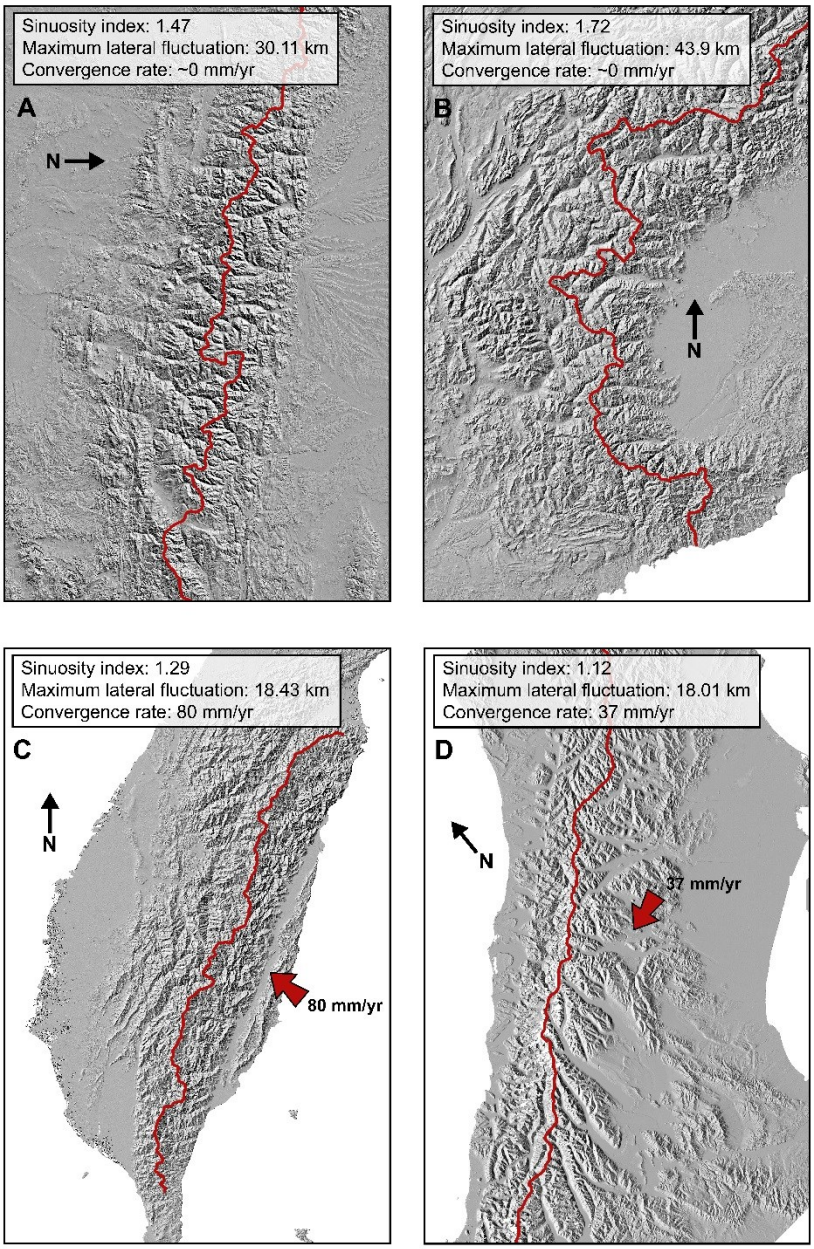

Figure 6 (2-columns, color): Comparison of the main actual drainage divide for mountain ranges shown at the same scale: A) Pyrenees, B) Western European Alps, C) Taiwan and D) Southern Alps of New Zealand, which all have similar dimensions. Red lines represent the main actual drainage divides and red arrows represent the rate and direction of convergence for the active systems of Southern Alps of the New Zealand and Taiwan.

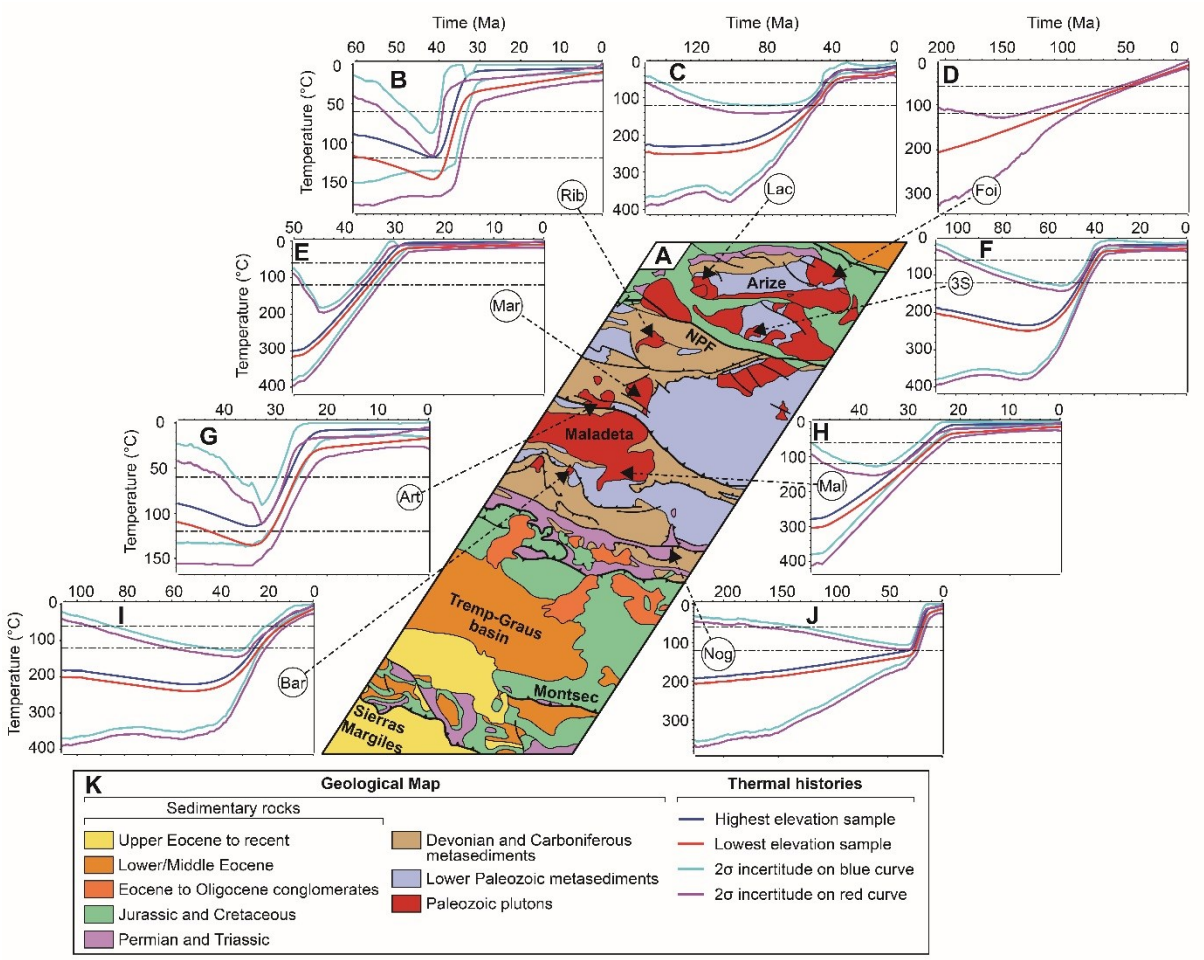

Figure 7 (2-columns, color): Complete set of thermal histories from the Central Pyrenees constructed from low-temperature thermochronology using QTQt. A) Detailed geological map of the Central Pyrenees around 1°E with location of different profiles used in this study. B-J) Set of thermal histories from the Central Pyrenees (sources of data are provided in supplementary tables 1 and 2). Thermal histories are built with the annealing models of Yamada et al., (2007) for ZFT data, Ketcham et al., (2007) for the AFT data and Gautheron et al., (2009) for AHe data. Red and blue curves are thermal histories for hottest (lowest elevation) and coldest (highest elevation) samples respectively. Magenta and cyan curves are 95% credible intervals for the red and blue curves, respectively. The difference between the thermal histories for the highest and lowest elevation samples is defined as the temperature-offset parameter, and is estimated assuming a range in temperature gradient of 15 to 45 °C/km. The thermal histories of the intermediate elevation samples are calculated by linear interpolation between the highest and lowest elevation thermal histories. K) Legend of geologic map and thermal histories.

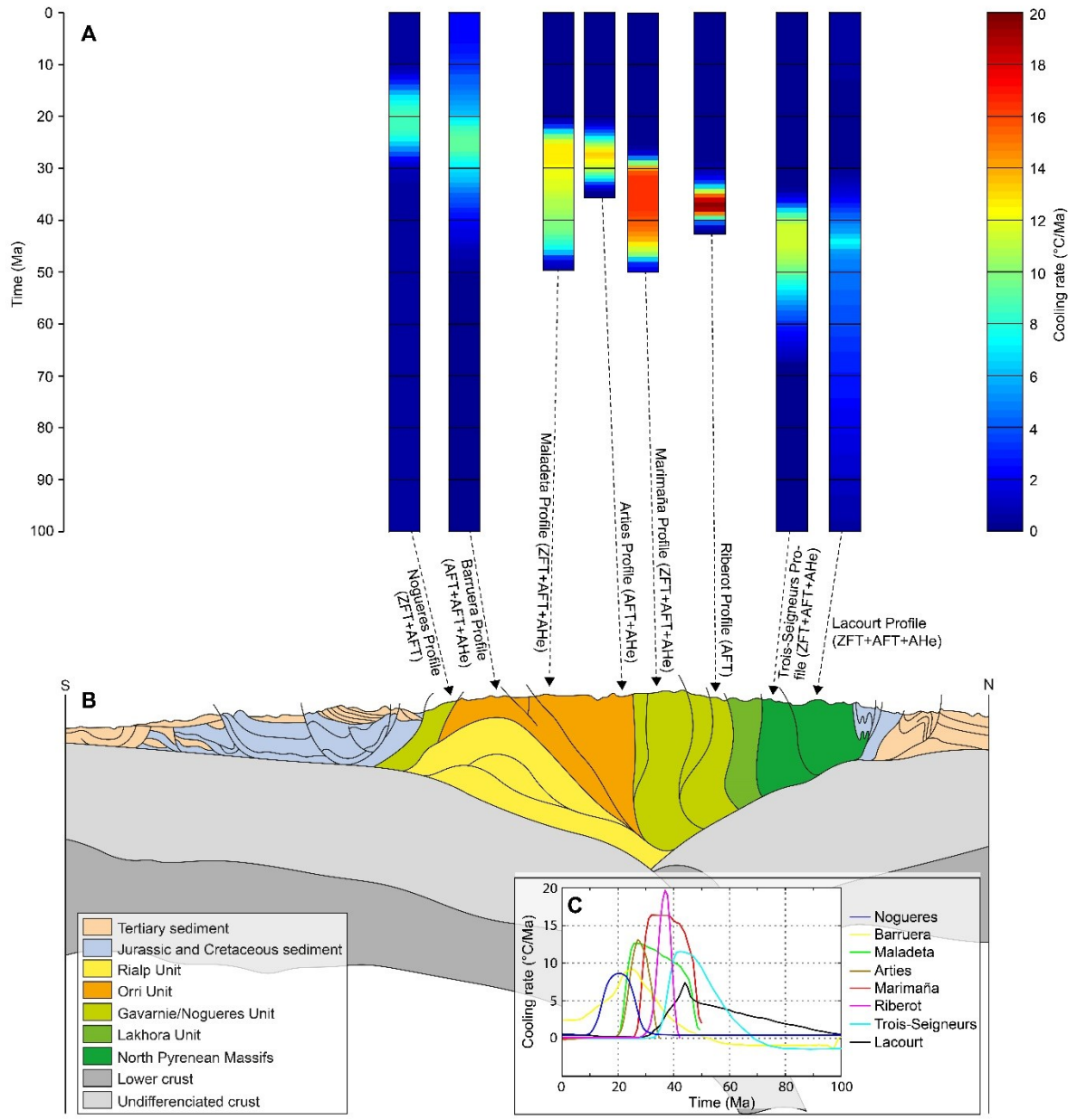

Figure 8 (2-columns, color): Cooling rate as a function of time along a north south transect in the Central Pyrenees. A) Colour representation of cooling rate build from the thermal histories as a function of time and according to the locality of each profile along the north south transect of the Central Pyrenees. Cooling rates are built from the QTQt thermal histories output. At each step-time (t_i, about every 1 Myrs), cooling rate is defined as the difference of temperature ($T_{i-1} - T_{i+1}$) divided by the difference of time ($t_{i-1} - t_{i+1}$). B) Geological north south cross-section (Beaumont et al., 2000 and Sinclair et al., 2005) along the ECORS profile in the Central Pyrenees. C) Cooling rate curves as a function of time for each profile.

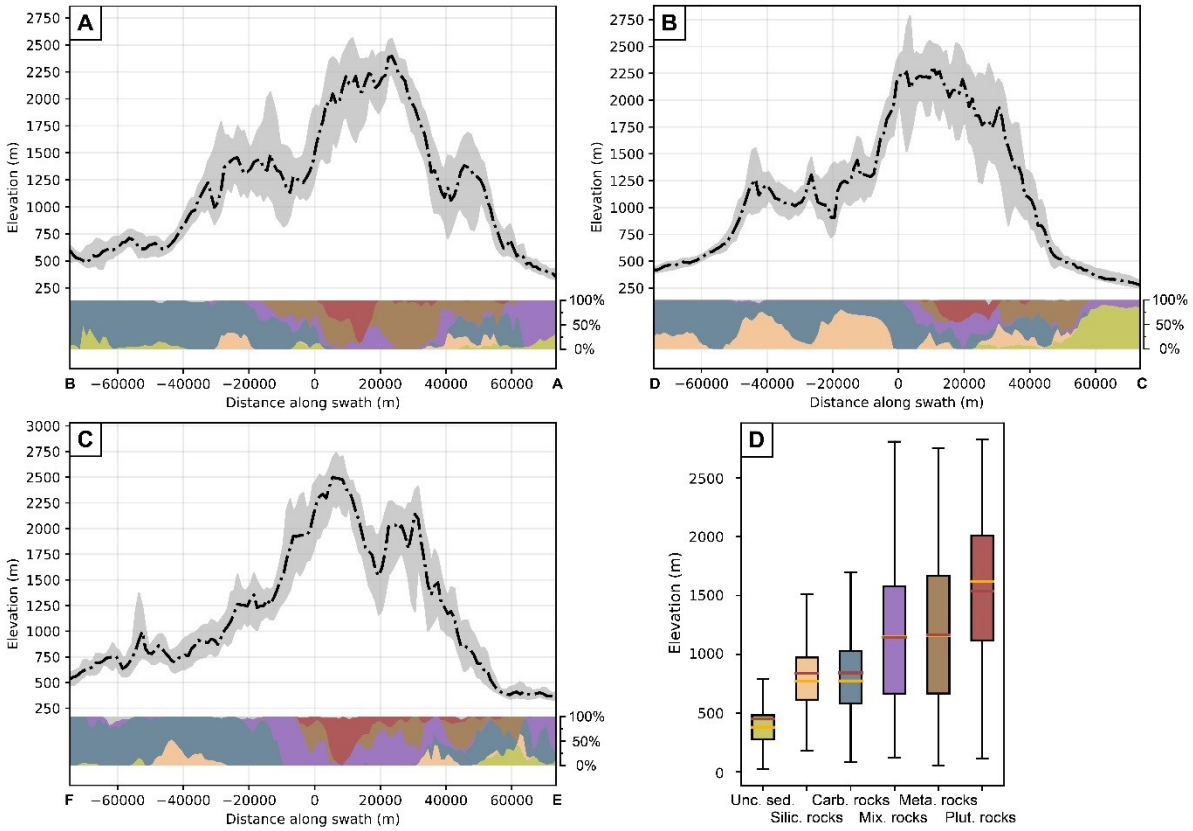

Figure 9 (2 columns, color): Topographic relation between elevation and lithology of the Pyrenees. A, B and C are transversal swath profiles of the Pyrenees (A) west; B) center; C) east). Dashed black line corresponds to the median elevation while the grey area corresponds to the elevation amplitude between the upper quartile elevation and lower quartile elevation. Color band below curve corresponds to the proportion of each lithology. Colors are the same as in panel D where the legend for lithology is indicated. D) Correlation between elevation and main lithology for the entire Pyrenees. Each box-and-whisker represent the minimal, 25th percentiles, 75th percentiles and maximal values in horizontal black lines while red and yellow horizontal lines represent respectively the mean and median values

Supplementary Material:

This supplementary material contains three tables about low-temperature thermochronological dataset used in this study and thermal history results. We present also height figures providing additional topographic analyses and inverse modelling information associated to this manuscript .

Sample	Location	Longitude	Latitude	Elevation	ZFTA	AFTA	AFTMTL	Reference
Mon-02/805	Nogueres	1.105	42.391	805	159	27.6	NaN	Sinclair et al., 2005
Mon-02/960	Nogueres	1.101	42.389	960	NaN	17.2	14.76	Sinclair et al., 2005
Mon-02/1085	Nogueres	1.097	42.388	1080	NaN	24.4	13.99	Sinclair et al., 2005
Mon-02/1280	Nogueres	1.092	42.386	1280	NaN	26.2	13.75	Sinclair et al., 2005
Bar-02/1150	Barruera	0.813	42.515	1150	104	21.4	13.18	Sinclair et al., 2005
Bar-02/1695	Barruera	0.808	42.52	1695	NaN	19.5	14.17	Sinclair et al., 2005
Bar-02/1780	Barruera	0.807	42.521	1780	Nan	21.2	13.95	Sinclair et al., 2005
Mal-00/1750	Maladeta	0.99	42.507	1750	49.3	28.96	13.73	Sinclair et al., 2005
Mal-00/2030	Maladeta	0.993	42.513	2030	NaN	27.7	13.88	Sinclair et al., 2005
Mal-00/2250	Maladeta	1.008	42.51	2250	NaN	28.5	14.02	Sinclair et al., 2005
Mal-00/2870	Maladeta	1.024	42.518	2870	NaN	33.1	14.27	Sinclair et al., 2005
ART/03/1315	Arties	0.872	42.677	1315	NaN	30.2	14.21	Gibson et al., 2007
ART/03/1555	Arties	0.867	42.675	1555	NaN	29.4	14.81	Gibson et al., 2007
ART/03/1880	Arties	0.862	42.675	1880	NaN	31.5	14.58	Gibson et al., 2007
ART/03/2164	Arties	8551	42.6728	2164	NaN	29.8	14.64	Gibson et al., 2007
Mar-00/2030	Marimana	0.976	42.705	2030	NaN	31.7	14.32	Sinclair et al., 2005
Mar-00/2200	Marimana	0.981	42.705	2200	NaN	27.6	14.28	Sinclair et al., 2005
Mar-00/2304	Marimana	0.983	42.706	2304	NaN	34.9	14.19	Sinclair et al., 2005
Mar-00/2440	Marimana	0.988	42.711	2440	NaN	38.6	14.19	Sinclair et al., 2005
Mar-00/2635	Marimana	0.993	42.714	2635	49.7	32.4	14.28	Sinclair et al., 2005
PY33	Riberot	1.05	42.806	1340	NaN	39	13.7	Fitzgerald et al., 1999
PY35	Riberot	1.052	42.808	1460	NaN	36	14.2	Fitzgerald et al., 1999
PY34	Riberot	1.0529	42.809	1595	NaN	37	14.7	Fitzgerald et al., 1999
PY39	Riberot	1.068	42.796	2050	NaN	41	NaN	Fitzgerald et al., 1999
PY38	Riberot	1.069	42.796	2205	NaN	42	14.5	Fitzgerald et al., 1999
PY37	Riberot	1.0725	42.797	2340	NaN	41	14.2	Fitzgerald et al., 1999
PY36	Riberot	1.0716	42.802	2483	NaN	44	14.2	Fitzgerald et al., 1999
3S-7	Trois-Seigneurs	1.441389	42.805278	1459	NaN	41.5	13.8	Vacherat et al., 2016
3S-6	Trois-Seigneurs	1.436944	42.812778	1598	NaN	41.8	13.6	Vacherat et al., 2016
3S-5	Trois-Seigneurs	1.435833	42.817778	1700	104.5	35.4	13.4	Vacherat et al., 2016
3S-4	Trois-Seigneurs	1.438611	42.820556	1772	100.8	37.6	14.2	Vacherat et al., 2016
3S-3	Trois-Seigneurs	1.440833	42.823611	1915	108.5	46.4	13.9	Vacherat et al., 2016
3S-2	Trois-Seigneurs	1.44	42.827222	2068	105.9	37	13.2	Vacherat et al., 2016
3S-1	Trois-Seigneurs	1.440278	42.830556	2199	153	46.5	14.1	Vacherat et al., 2016
Lac-1	Lacourt	1.176667	42.934167	451	155.6	43.9	13.5	Vacherat et al., 2016
Lac-2	Lacourt	1.213611	42.907778	493	135	38.5	13.5	Vacherat et al., 2016
PY6	Lacourt	1.215	42.94028	645	NaN	49	14.1	Fitzgerald et al., 1999
PY7	Lacourt	1.20222	42.9425	815	NaN	50	13.9	Fitzgerald et al., 1999
PY3	Lacourt	1.21417	42.93306	950	NaN	49	13.4	Fitzgerald et al., 1999
PY2	Lacourt	1.13306	42.93306	1048	NaN	55	13.7	Fitzgerald et al., 1999
Foi-1	Foix	1.532778	42.964444	488	168	74.9	13	Vacherat et al., 2016

Supplementary Table 1: List of apatite and zircon fission track analytical data in the Central Pyrenees used for this study. (i) Longitude and latitude are in degree decimal unit. (ii) ZFTA and AFTA correspond respectively to zircon fission track age and apatite fission track age. AFTMTL corresponds to apatite fission track mean track length.

Sample	Location	Longitude	Latitude	Elevation	AHeA	Reference
BAR/02/1150-2	Barruera	0.813	42.515	1150	10.5	Gibson et al., 2007
BAR/02/1695-2	Barruera	0.808	42.52	1695	13.8	Gibson et al., 2007
BAR/02/1150-3	Barruera	0.813	42.515	1695	15.9	Gibson et al., 2007
MAL/00/1750-1	Marimana	0.99	42.507	1750	23.4	Gibson et al., 2007
MAL/00/1750-2	Marimana	0.99	42.507	1750	22.9	Gibson et al., 2007
MAL/00/1750-3	Marimana	0.99	42.507	1750	23.9	Gibson et al., 2007
MAL/00/1920-1	Marimana	0.994	42.511	1920	27.9	Gibson et al., 2007
MAL/00/1920-2	Marimana	0.994	42.511	1920	22.8	Gibson et al., 2007
MAL/00/2030-1	Marimana	0.993	42.513	2030	20.8	Gibson et al., 2007
MAL/00/2030-2	Maladeta	0.993	42.513	2030	26.8	Gibson et al., 2007
MAL/00/2140-3	Maladeta	1.001	42.51	2140	30.2	Gibson et al., 2007
MAL/00/2250-1	Maladeta	1.008	42.51	2250	24.5	Gibson et al., 2007
MAL/00/2250-2	Maladeta	1.008	42.51	2250	31.3	Gibson et al., 2007
MAL/00/2360-1	Maladeta	1.013	42.512	2360	24	Gibson et al., 2007
MAL/00/2440-6	Maladeta	1.02	42.511	2440	26.1	Gibson et al., 2007
MAL/00/2650-3	Maladeta	1.025	42.513	2650	32.6	Gibson et al., 2007
MAL/00/2650-4	Maladeta	1.025	42.513	2650	30.8	Gibson et al., 2007
MAL/00/2650-5	Maladeta	1.025	42.513	2650	31.4	Gibson et al., 2007
MAL/00/2765-1	Maladeta	1.025	42.514	2765	34.9	Gibson et al., 2007
MAL/00/2765-2	Maladeta	1.025	42.514	2765	20.4	Gibson et al., 2007
MAL/00/2870-1	Maladeta	1.024	42.518	2870	29.2	Gibson et al., 2007
MAL/00/2870-2	Maladeta	1.024	42.518	2870	26.4	Gibson et al., 2007
MAL/00/2870-7	Maladeta	1.024	42.518	2870	17.3	Gibson et al., 2007
ART/03/1480-2	Arties	0.8677	42.6734	1480	27.5	Gibson et al., 2007
3S-1/A	Trois Seigneurs	1.4401	42.8305	2199	41.3	Vacherat et al., 2014
3S-1/B	Trois Seigneurs	1.4401	42.8305	2199	47	Vacherat et al., 2014
3S-1/C	Trois Seigneurs	1.4401	42.8305	2199	40.9	Vacherat et al., 2014
3S-1/D	Trois Seigneurs	1.4401	42.8305	2199	42.4	Vacherat et al., 2014
3S-2/A	Trois Seigneurs	1.44	42.8272	2068	31.1	Vacherat et al., 2014
3S-2/B	Trois Seigneurs	1.44	42.8272	2068	34.2	Vacherat et al., 2014
3S-2/C	Trois Seigneurs	1.44	42.8272	2068	35.7	Vacherat et al., 2014
3S-2/D	Trois Seigneurs	1.44	42.8272	2068	35.1	Vacherat et al., 2014
3S-3/A	Trois Seigneurs	1.4409	42.8235	1915	37	Vacherat et al., 2014
3S-3/B	Trois Seigneurs	1.4409	42.8235	1915	43.2	Vacherat et al., 2014
3S-3/C	Trois Seigneurs	1.4409	42.8235	1915	44.3	Vacherat et al., 2014
3S-3/D	Trois Seigneurs	1.4409	42.8235	1915	38	Vacherat et al., 2014
3S-3/E	Trois Seigneurs	1.4409	42.8235	1915	35.4	Vacherat et al., 2014
3S-4/A	Trois Seigneurs	1.4387	42.8206	1772	37.8	Vacherat et al., 2014
3S-5/A	Trois Seigneurs	1.4357	42.8179	1700	34	Vacherat et al., 2014
3S-5/B	Trois Seigneurs	1.4357	42.8179	1700	33.4	Vacherat et al., 2014
3S-5/C	Trois Seigneurs	1.4357	42.8179	1700	33.9	Vacherat et al., 2014
3S-5/D	Trois Seigneurs	1.4357	42.8179	1700	32.7	Vacherat et al., 2014
3S-6/A	Trois Seigneurs	1.4371	42.8128	1598	47.6	Vacherat et al., 2014
3S-6/B	Trois Seigneurs	1.4371	42.8128	1598	55.8	Vacherat et al., 2014
3S-6/C	Trois Seigneurs	1.4371	42.8128	1598	49	Vacherat et al., 2014
3S-7/A	Trois Seigneurs	1.4415	42.8054	1459	36.9	Vacherat et al., 2014
3S-7/B	Trois Seigneurs	1.4415	42.8054	1459	37.4	Vacherat et al., 2014
3S-7/C	Trois Seigneurs	1.4415	42.8054	1459	33	Vacherat et al., 2014
3S-7/D	Trois Seigneurs	1.4415	42.8054	1459	38.1	Vacherat et al., 2014
Lac-1/A	Lacourt	1.1768	42.9341	451	36.5	Vacherat et al., 2014
Lac-1/B	Lacourt	1.1768	42.9341	451	37.6	Vacherat et al., 2014
Lac-1/C	Lacourt	1.1768	42.9341	451	37.9	Vacherat et al., 2014
Lac-1/D	Lacourt	1.1768	42.9341	451	29.9	Vacherat et al., 2014
Lac-2/A	Lacourt	1.2137	42.9078	493	37.2	Vacherat et al., 2014
Lac-2/B	Lacourt	1.2137	42.9078	493	27.7	Vacherat et al., 2014
Lac-2/D	Lacourt	1.2137	42.9078	493	36.7	Vacherat et al., 2014
Foi-1/A	Foix	1.5328	42.9646	488	34.5	Vacherat et al., 2014
Foi-1/B	Foix	1.5328	42.9646	488	50.9	Vacherat et al., 2014
Foi-1/C	Foix	1.5328	42.9646	488	55	Vacherat et al., 2014

Supplementary Table 2: List of apatite helium analytical data in the Central Pyrenees used for this study. (i) Longitude and latitude are in degree decimal unit. (ii) AHeA corresponds to apatite helium age.

Profile	Decrease cooling rate timing (Ma)	Cooling rate decrease time (Myrs)	Rate of cooling change (°C.Myrs^{-2})
Lacourt	30	15	0.7±0.1
Trois-Seigneurs	33	10	0.4±0.1
Riberot	28	9	1.8±0.3
Marimaña	25	7	1.5±0.1
Arties	20	9	2.4±0.3
Maladeta	20	7	2.0±0.2
Barruera	7	19	1.2±0.1
Nogueres	10	11	0.5±0.1

Supplementary Table 3: Summary of results from the thermal histories for each elevation profiles from north to south.

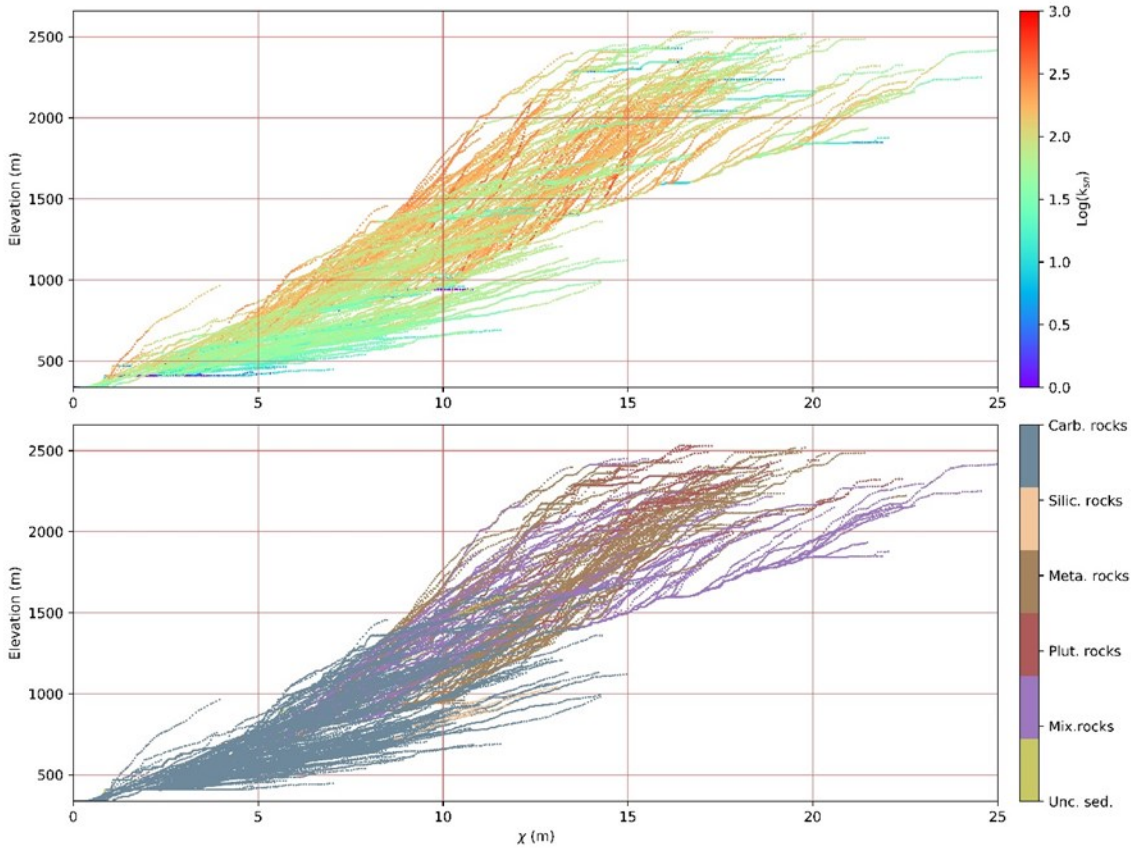

Supplementary Figure 1 (2 columns): Long profile χ-elevation plots for the Noguera Pallaresa catchment. Colors correspond to the log of k_{sn} for the upper panel and to lithology for the lower panel. Plots highlight channels influenced by glacial erosion at high altitudes and characterized by a break in long profile and low k_{sn} values. Low k_{sn} values (blue colors) in lower panel suggest glacial influence becomes more pronounced above 1900 meters elevation. Metamorphic and plutonic rocks are the lithologies principally affected by glacial effect.

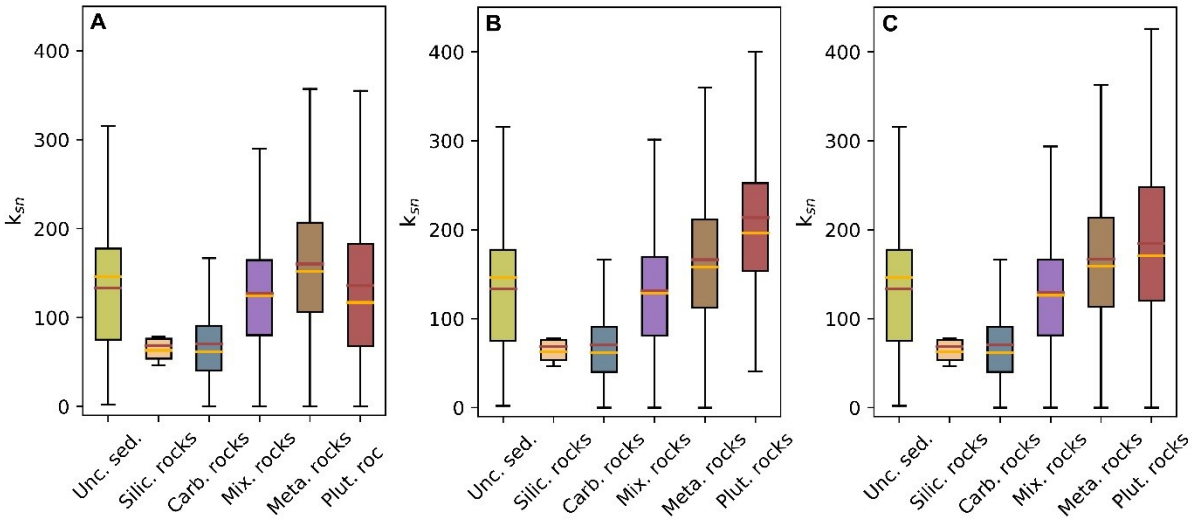

Supplementary Figure 2 (2 columns): Relation between lithologies and channel steepness for Noguera Pallaresa catchment with A) no consideration of potential glacial effect on channel steepness; B) consideration of glacial effect with removal of k_{sn} values above 1900 m; C) consideration of glacial effect with removal of k_{sn} values above 2100 m. Note highest mean and median k_{sn} values for plutonic rocks in panel B and C when removing k_{sn} values above a limit elevation. Each box-and-whisker represent the minimal, 25th percentiles, 75th percentiles and maximal values in horizontal black lines while red and yellow horizontal lines represent respectively the mean and median values

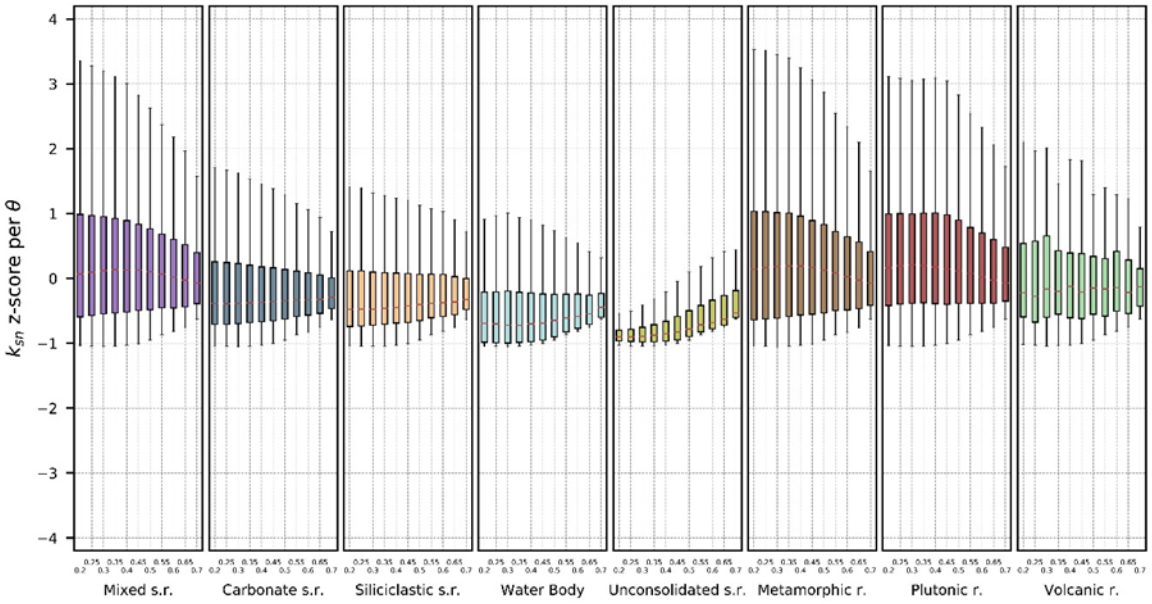

Supplementary Figure 3 (2-columns): k_{sn} z-score associated to the different lithologies as a function of different θ which correspond to the m/n ratio. From left to right each graphic plot corresponds to the k_{sn} z-score for different m/n ratio (0.2, 0.25, 0.3, 0.35, 0.4, 0.45, 0.5, 0.55, 0.6, 0.65 and 0.7) for each lithology (mixed sedimentary rocks, carbonate sedimentary rocks, siliciclastic sedimentary rocks, water body, unconsolidated sedimentary rocks, metamorphic rocks, plutonic rocks and volcanic rocks). The standard score or z-score corresponds to the number of standard deviations by which the value data is above or under the mean value. Z-score = $(x - \mu)/\sigma$ where μ is the mean and σ is the standard deviation.

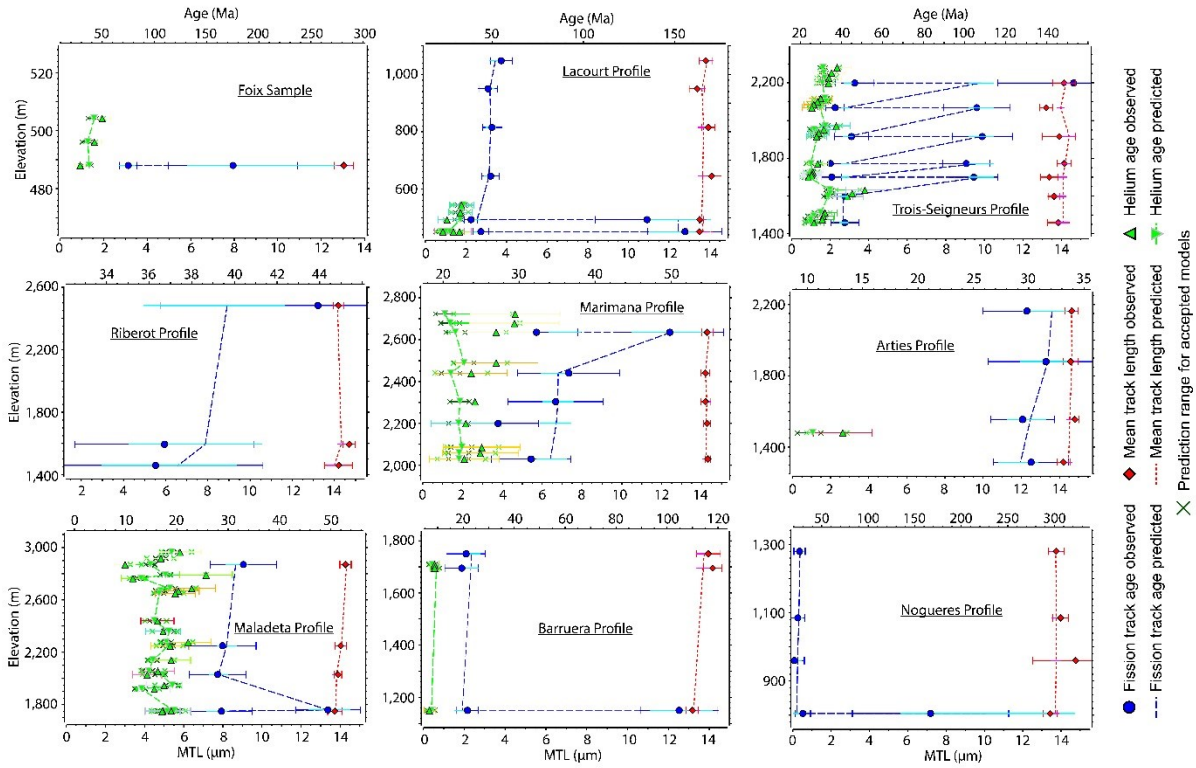

Supplementary Figure 4 (2-columns): Complete set of predictions from thermal history models compared to observed data. The predicted and observed values for all samples in the profiles are represented as a function of elevation. Normal green triangles, blue circles and red diamonds are respectively AHe ages, FT ages and mean track length (MTL) observed. Errors bars on AHe ages, FT ages and MTL are included and are represented by green, blue and red horizontal lines. Inverse green triangles, blue vertical lines and red vertical lines are the predicted AHe ages, FT ages and MTL respectively. The cyan, magenta, and green horizontal lines are the mean and 95% credible range for the predictions on FT ages, MTL and AHe ages, respectively. Green crosses correspond to the helium prediction range for accepted models. Yellow squares and horizontal lines are the prior kinetic parameters and error bars (multi-composition model of Ketcham et al., 2007 for apatite fission tracks data, Yamada, 2007 for zircon fission track data and the models of Gautheron et al., 2009 and Flowers et al., 2009 for helium data) used as inputs for inverse modelling. Yellow vertical lines are the predicted kinetic parameters while the modelled 95% credible range is shown as light yellow horizontal lines.

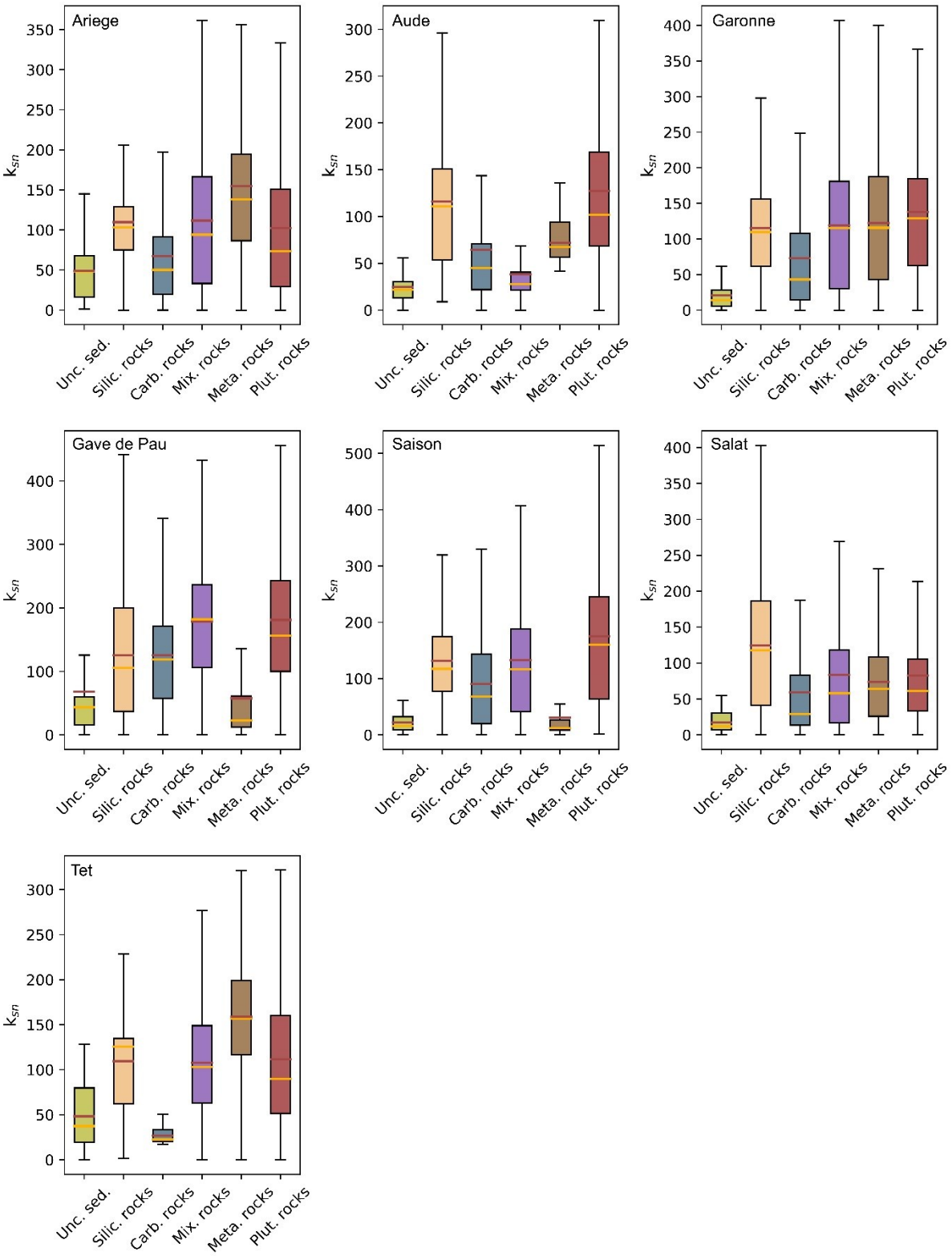

Supplementary Figure 5 (2-columns): Complete set of box and whisker plots of the range of k_{sn} values associated with each lithology for the catchments of the northern Pyrenees. The different catchments are Saison, Gave de Pau, Garonne, Salat, Ariège, Aude and Tet. Colors of boxplots and lithology abbreviations are in accord with figures 2 and 4. Each box-and-whisker represent the minimal, 25th percentiles, 75th percentiles and maximal values in horizontal black lines while red and yellow horizontal line represent respectively the mean and median values.

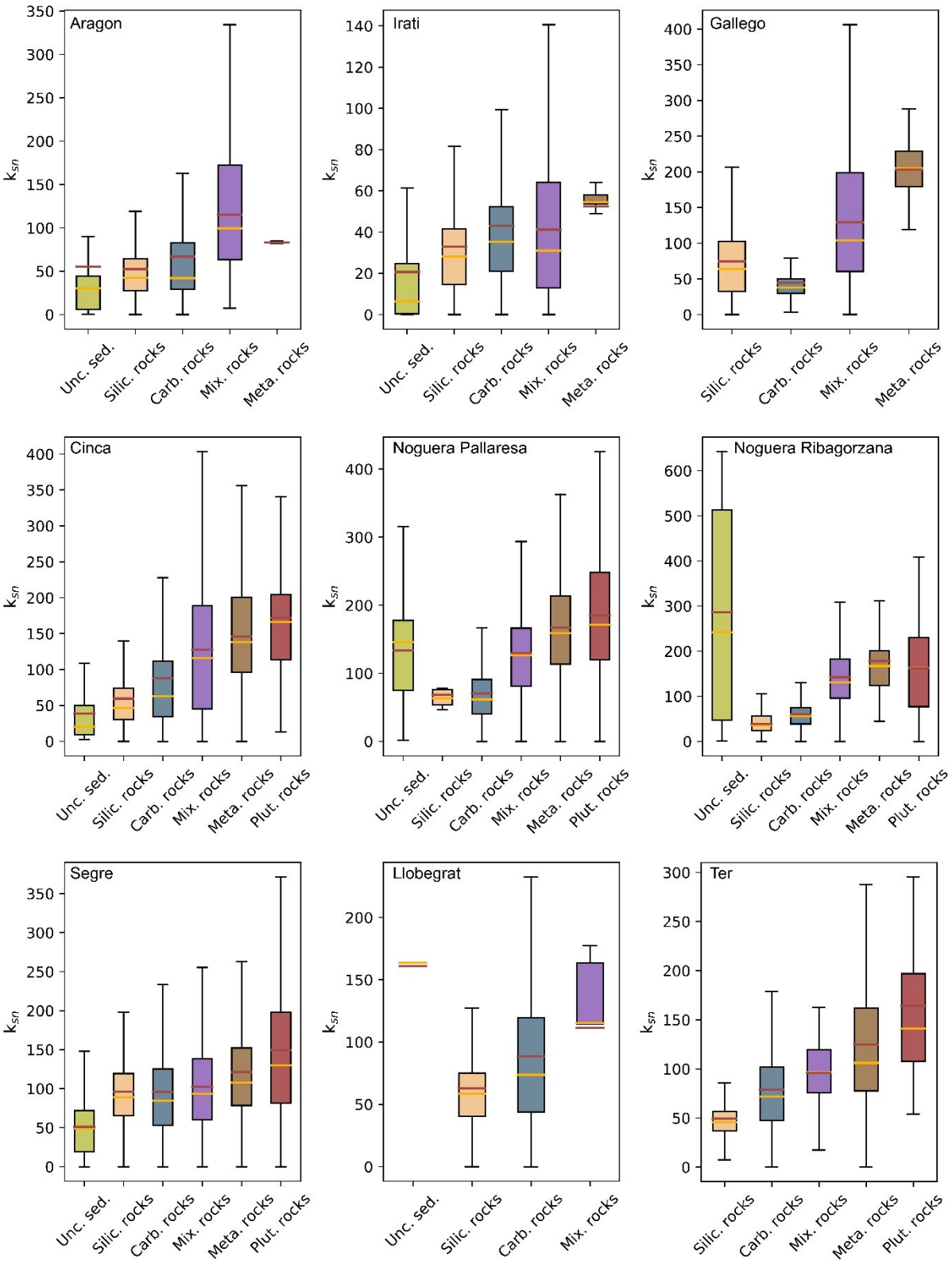

Supplementary Figure 6 (2-columns): Complete set of box and whisker plot of the range of ksn values associated with each lithology for the main catchments of the southern Pyrenees. The different catchments are Irati, Aragon, Gallego, Cinca, Noguera Ribagorzana, Noguera Pallaresa, Segre, Llobegrat and Ter. Each box-and-whisker represent the minimal, 25th percentiles, 75th percentiles and maximal values in horizontal black lines while red and yellow horizontal line represent respectively the mean and median values.

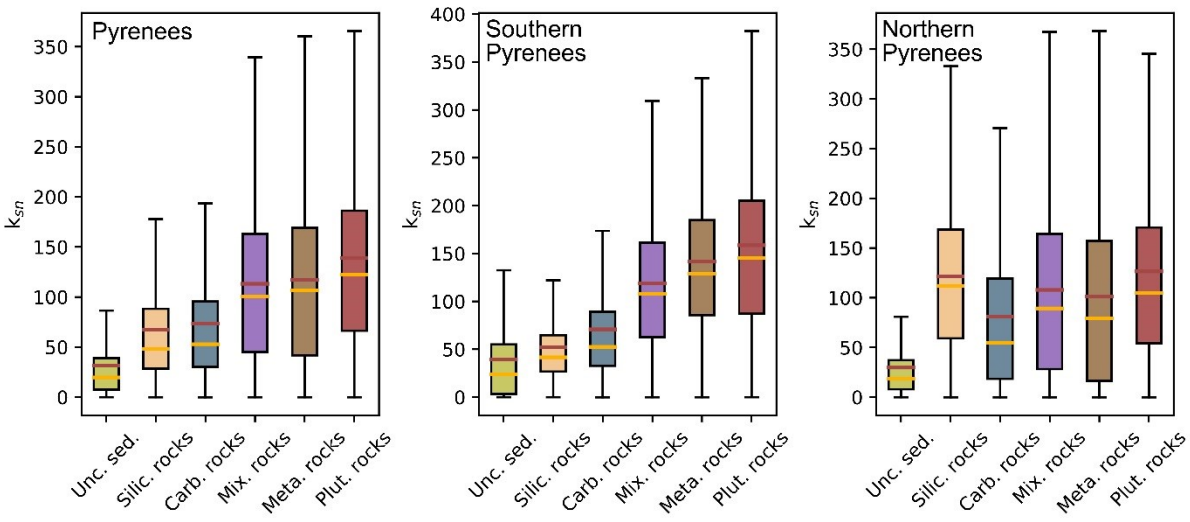

Supplementary Figure 7 (2-columns): Set of box and whisker plot of the range of k_{sn} values associated to each lithology for the entire Pyrenees, northern Pyrenees and southern Pyrenees. The northern Pyrenees corresponds to Ariège, Aude, Garonne, Gave de Pau, Saison, Salat and Tet catchments. The southern Pyrenees corresponds to Aragon, Cinca, Gallego, Irati, Llobegrat, Noguera Pallaresa, Noguera Ribagorzana, Segre and Ter catchments. Each box-and-whisker represents the minimal, 25th percentiles, 75th percentiles and maximal values in horizontal black lines while red and yellow horizontal lines represent respectively the mean and median values.

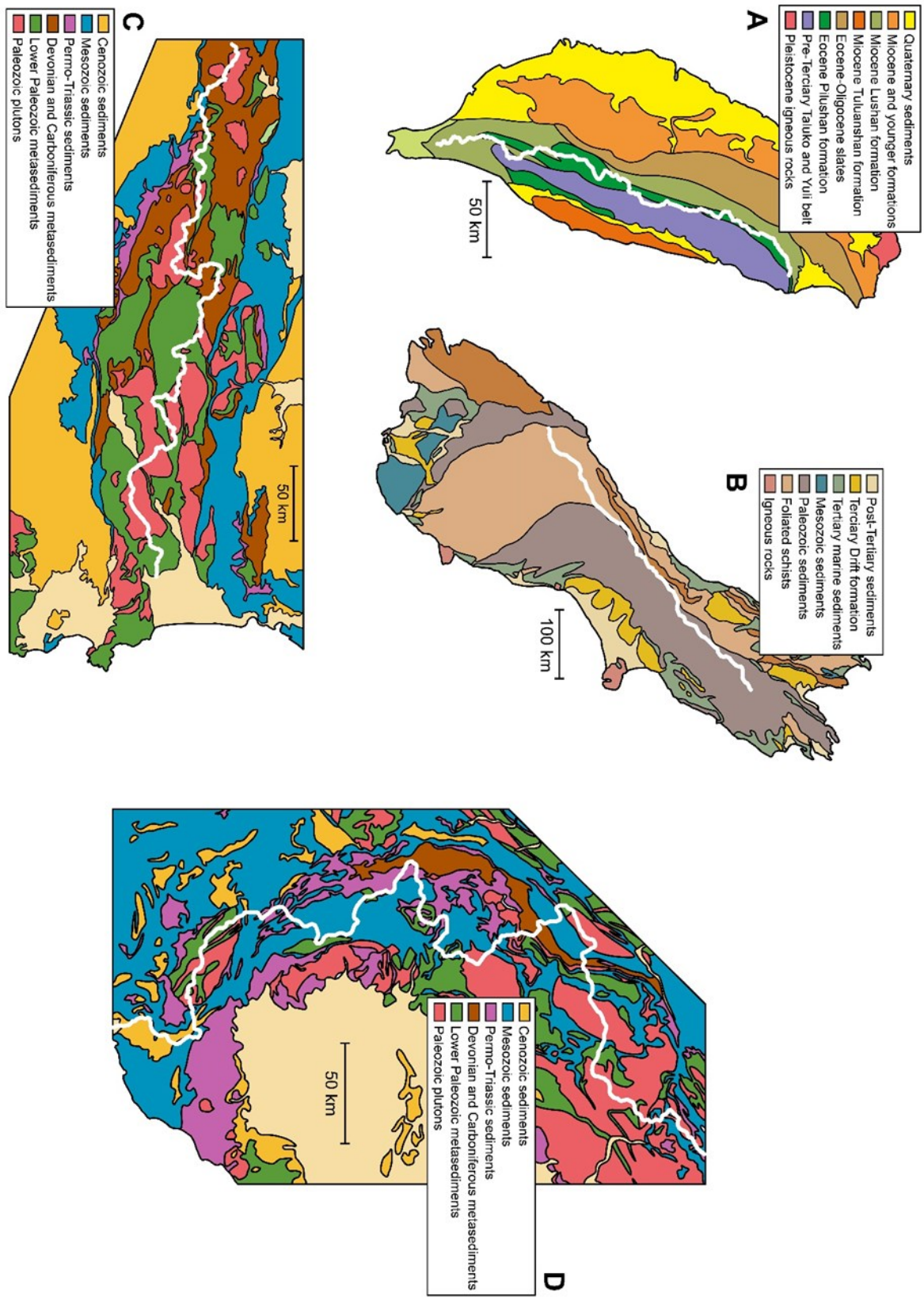

Supplementary Figure 8 (2-columns): Geologic map of A) Taiwan, B) Southern Alps of New Zealand, C) Pyrenees and D) Western European Alps showing the relation between the main drainage divide and the lateral variation of geologic units. Scale is not respected between the different orogens.